

Solfrid Hagen Johansen

The Isotropic Hyperfine Interaction in Silicon Quantum Dots

Master's thesis in Applied Physics and Mathematics

Supervisor: Jon Andreas Støvneng (IFY)

Co-supervisor: Trond Brudevoll (FFI)

August 2021

Solfrid Hagen Johansen

The Isotropic Hyperfine Interaction in Silicon Quantum Dots

Master's thesis in Applied Physics and Mathematics
Supervisor: Jon Andreas Støvneng (IFY)
Co-supervisor: Trond Brudevoll (FFI)
August 2021

Norwegian University of Science and Technology
Faculty of Natural Sciences
Department of Physics



To my family

Abstract

Quantum computing can, in theory, perform certain calculations that are infeasible to perform on classical computers. A limiting factor for utilizing quantum computers is the decoherence time of the qubit, as this limits the number of computations that may be performed. Here we investigate the decoherence due to hyperfine interactions, expressed through hyperfine parameters, in electron spin-based qubits confined in silicon quantum dots. We do this by applying density functional theory using the Perdew, Burke and Ernzerhof, and modified Becke-Johnson exchange-correlation functionals, as implemented in the program WIEN2k. The main goal is to compute the isotropic hyperfine parameter using the procedure utilized by Assali *et al.*[Phys. Rev. B 83, 165301(2011)], and provide further details on the computation. The hyperfine parameters are theoretically derived and are obtained from supercells of varying sizes for bulk silicon containing a single extra electron placed in one of the six conduction band minima. From the isotropic hyperfine parameter of bulk silicon, we obtain a decoherence time for a quantum dot in natural silicon of $T_2^* = 0.25 \mu\text{s}$ using the modified Becke-Johnson potential.

Sammendrag

Kvantedatamaskiner kan i teorien utføre visse beregninger som ikke er mulig å utføre på klassiske datamaskiner. En begrensende faktor for bruk av kvantedatamaskiner er dekoherenstiden til en kvantebit (qubit), da dette begrenser antall beregninger som kan utføres. Her undersøker vi dekoherensen forårsaket av hyperfine vekselvirkninger, uttrykt gjennom hyperfine parametere, i elektronspinn-baserte qubits i silisium kvanteprikker. Vi gjør dette ved å bruke tetthetsfunksjonal teori ved bruk av PBE- og mBJ-utvekslingskorrelasjonsfunksjonalen, som implementert i programmet WIEN2k. Hovedmålet er å beregne den isotrope hyperfine parameteren ved å benytte fremgangsmåten fra Assali *et al.* [Phys. Rev. B 83, 165301 (2011)], og vi presenterer ytterligere detaljer rundt beregningen. De hyperfine parametrene er teoretisk utledet og er funnet fra superceller av ulike størrelser for silisium som inneholder et enkelt ekstra elektron plassert i ett av de seks ledningsbånd-minima. Fra den isotrope hyperfine parameteren til silisium finner vi en dekoherenstid for en kvanteprikk i naturlig silisium på $T_2^* = 0.25 \mu\text{s}$ ved bruk av mBJ utvekslingskorrelasjonsfunksjonalen.

Preface

This thesis concludes my Master of Science degree in Applied Physics and Mathematics at the Department of Physics at the Norwegian University of Science and Technology (NTNU). The work was done during the spring semester of 2021. In the fall of 2020, I wrote a literature review of electron spin qubits in silicon quantum dots as my specialization project. Some parts of the theory are therefore identical (or nearly identical) to the project report.

I want to thank my supervisor Trond Brudevoll at the Norwegian Defence Research Establishment/Forsvarets forskningsinstitutt (FFI), for guiding me and supporting me when working with the thesis. I am very grateful for his positive mindset and belief in me through working with him over the past year. Thank you to Ida Breivik, a summer employee at FFI, for helping me with setting up the largest supercells and performing computations in parallel. I would also like to thank my family and friends for their support and encouragement.

Contents

Abstract	iii
Sammendrag	v
Preface	vii
Contents	ix
List of Tables	xiii
List of Figures	xv
Abbreviations	xviii
1 Introduction	1
1.1 Aim and Approach	2
1.2 Thesis Contents	2
2 Theory	5
2.1 Quantum Computing	5
2.1.1 Quantum Bits	5
2.1.2 Quantum Circuits	7
2.1.3 Physical Realization of Quantum Computers	11
2.2 Electron Spin Qubits	14
2.2.1 Quantum Dots	14
2.2.2 Spin States in a Single Quantum Dot	15
2.3 Control Techniques	17
2.3.1 Electron Spin Resonance	17

2.3.2	Electron Spin Resonance for Manipulation of Spin States . . .	19
2.3.3	EDSR for Qubit Control	20
2.4	Solid State Physics	22
2.5	Silicon for Quantum Technologies	23
2.6	Hyperfine Interactions	25
2.6.1	Derivation of the Hyperfine Interactions From the Dirac Equation	25
2.6.2	Derivation of the Hyperfine Interaction Parameters for an Axial Symmetric System	29
2.6.3	Hyperfine Parameters for a Silicon Quantum Dot With an Additional Electron	31
2.7	Density Functional Theory	33
2.7.1	Kohn-Sham Equations	33
2.7.2	Solving the Kohn-Sham Equations	35
2.7.3	Basis Functions in DFT	36
2.7.4	Exchange-Correlation Functionals	39
3	Method	41
3.1	WIEN2k	41
3.1.1	DFT Implementation	41
3.1.2	Initializing a Calculation	42
3.1.3	Running an SCF cycle	44
3.1.4	Spin-Polarized Calculations	45
3.1.5	Spin-Orbit Coupling	45
3.1.6	Creating Supercells	46
3.1.7	Calculating Band Structure Using Spaghetti	47
3.1.8	Charged Supercells	47
3.1.9	Using the Modified Becke-Johnson XC-Potential	48
3.1.10	Computing the Contact Hyperfine Interaction	48
3.1.11	Producing Density Plots Using LAPW5	49
3.1.12	Numerical Considerations	49
3.2	Bulk Silicon Computations	50
3.3	Isotropic Hyperfine Interaction	51

3.4	Isotropic Hyperfine Interaction in a Silicon Quantum Dot	54
3.5	Visualizing the Spin-Density	54
4	Results	55
4.1	Bulk Silicon	55
4.2	Isotropic Hyperfine Parameter for Silicon Supercells	57
4.3	Isotropic Hyperfine Parameter for a Silicon Quantum Dot	59
4.4	Visualizing the Spin-Density	61
5	Discussion	63
6	Conclusions	67
6.1	Further Work	67
	Bibliography	69
	Appendices	77
A	Details of the Computations	77
A.1	Structure File for Silicon	77
A.2	Numerical Procedure for Bulk Silicon	78
A.3	k -mesh Convergence Test	78
A.4	$R_{mt}K_{max}$ Convergence Test	79
A.5	Computation Using the mBJ XC-Potential	79
A.6	Procedure for Computing the Isotropic Hyperfine Interaction	80
A.7	case.output2up/dn	82
B	Input Files	85
B.1	case.inso	85
B.2	case.klist_band	85
B.3	case.insp	88
B.4	case.in5	88
C	Supercells	91
C.1	8-atom Supercell	91
C.2	16-atom Supercell	93

C.3	32-atom Supercell	94
C.4	54-atom Supercell	95
C.5	64-atom Supercell	98
D	Convergence Tests	103

List of Tables

4.1	Computed isotropic hyperfine parameters.	58
4.2	Computed hyperfine parameters a where N is the number of atoms in the supercell, using the mBJ potential.	60
4.3	Slope of the linear interpolation, such that the value for a supercell containing N atoms is x/N , with $x = a, a_{r_T}$ for the PBE and mBJ-XC potentials.	60
4.4	Computed values of η for the PBE and mBJ potentials for both ρ_s and ρ_{s,r_T}	61
5.1	Values of the parameter η obtained experimentally and theoretically using different methods.	66

List of Figures

2.1	Visualization of an arbitrary quantum state on a Bloch sphere.	8
2.2	Schematic picture of a lateral quantum dot structure.	15
2.3	Visualization of the spins of the singlet and triplet states, with the energy levels shown.	17
2.4	Visualization on a Bloch sphere of the precession of the state vector about $\mathbf{B}_0 = B_0 \hat{z}$	18
3.1	Visual summary of the procedure used for computing the HFI parameters for silicon supercells with one additional electron placed in the conduction band minima.	52
4.1	a) Total energy with respect to the number of k -points in the IBZ. b) Total energy with respect to $R_{mt}K_{max}$	55
4.2	Band structure of silicon using the PBE XC-potential	56
4.3	Computed values of a and a_{r_T} as a function of $1/N$ together with the interpolated values using the PBE XC-potential.	58
4.4	Computed values of a and a_{r_T} as a function of $1/N$ together with the interpolated values using the mBJ XC-potential.	59
4.5	Computed values of η for both the PBE and mBJ XC-potentials using the density computed at the nucleus and the average over the Thomson radius.	60
4.6	Spin-densities of silicon with one additional electron, in two different planes.	62
C.1	Visualization of the supercells from $N = 8$ to $N = 64$ used for the computations.	101

D.1 Computed values for a , with respect to the number of k -points in the
IBZ for supercells containing from $N = 8$ to $N = 64$ atoms. 104

Abbreviations

1BZ - First Brillouin zone
APW - Augmented plane wave
BZ - Brillouin zone
DFT - Density functional theory
EDSR - Electric-dipole spin resonance
ESR - Electron spin resonance
fcc - Face centered cubic
GGA - Generalized gradient approximation
HFI - Hyperfine interaction
IBZ - Irreducible Brillouin zone
KS - Kohn-Sham
LAPW - Linearized augmented plane wave
LDA - Local density approximation
lo/LO - Local orbital
mBJ - Modified Becke Johnson
NMR - Nuclear magnetic resonance
PBE - Perdew, Burke, and Ernzerhof
QC - Quantum computer
QD - Quantum dot
RF - Radio frequency
SCF - Self-consistent field
SOC - Spin-orbit coupling
SOI - Spin-orbit interaction
UG - User guide
XC - Exchange-correlation

Chapter 1

Introduction

Quantum computing uses principles from quantum mechanics and can, in theory, perform calculations that are infeasible to perform on classical computers[1]. Quantum computers are based on qubits, which are the quantum analog to classical bits, and can be in a superposition of two quantum states. A qubit must be physically implemented as a two-level quantum system, and several implementations are currently being studied and developed[2–4]. When one considers a two-level quantum system, one natural choice is the electron spin. An electron spin can represent the classical 0 and 1 bit values through the quantum states known as "up" and "down"[5]. Electron spin qubits in silicon quantum dots have reached the point where the level of control and coherence makes them exciting candidates for quantum processors in the near future[6–10]. In addition, there is already a huge industry surrounding silicon for classical processors.

Qubits need to be coherent over a certain amount of time, meaning that information on the quantum state cannot be lost to random state-fluctuations, to allow for performing computations on them[11]. In electron spin qubits, the main cause of fluctuations is due to the hyperfine interactions with finite-spin nuclei in the surroundings[12–14]. Silicon has an advantage as a host material due to the low abundance of the finite-spin isotope ^{29}Si in natural silicon. Although a low abundance, the effect of these isotopes on the coherence time needs to be accurately assessed to determine the finite time for which the spins can be used for computations. Therefore, the coherence time dictates what kind of computations may be performed. Recently the hyperfine interaction in silicon has been utilized to con-

trol single Si^{29} spins[15], which demonstrates that the hyperfine interaction should be known to eliminate the unwanted effects, and possibly take advantage of the coupling with the spin.

1.1 Aim and Approach

In this thesis, the isotropic hyperfine interaction for electron spins confined to a silicon quantum dot is computed using density functional theory, as implemented in WIEN2k[16]. The procedure is based on work done by Assali *et al.*[14]. The hyperfine parameter is then translated into a random Overhauser field, an unknown and random field, which is used to compute the dephasing time, T_2^* , of the electron.

The hyperfine interactions in an axially symmetric system can be expressed through two parameters, a and b , which depend on the spin-density, $\rho_s = \rho_\uparrow - \rho_\downarrow$. The procedure used to compute the parameters are based on supercells with an extra electron for a single k -value and placed in the conduction band. By computing the parameters for different sized supercells, a scaling is achieved, which again is used to compute hyperfine interactions for a quantum dot by using the envelope function approximation. It should be emphasized that this is the same procedure used by Ref. [14], but this thesis offers details on the computations which are not explained in their article. In addition, the computations here are also performed for the modified Becke-Johnson exchange-correlation potential.

The main goal is to explain in detail the procedure used in WIEN2k to compute the isotropic parameter, a , in order to obtain an estimated decoherence time due to the hyperfine interactions. We also compare the results using the PBE XC-potential with the obtained results using a different XC-potential. In addition, we present computations for regular bulk silicon to confirm the well-known properties of the element.

1.2 Thesis Contents

The thesis is written for an audience with a knowledge of basic quantum mechanics and numerical methods. The report is structured as follows:

- **Chapter 2** presents the theory behind quantum computing, hyperfine interactions, solid-state physics, and density functional theory
- **Chapter 3** introduces the parts of the program WIEN2k which are relevant for the computations. Further, the method used to perform a standard computation for silicon is presented, and finally, the method used for computing the isotropic hyperfine parameter for a conduction electron in a silicon quantum dot.
- **Chapter 4** presents the results for bulk silicon and the isotropic parameter, along with visualizations of the spin-density.
- **Chapter 5** discusses the results obtained.
- **Chapter 6** concludes the thesis and suggests further work.

Chapter 2

Theory

In this section the theory behind quantum computing and spin based qubits is discussed. Fundamental concepts from solid state physics are presented. Further, the Kohn-Sham equations used in density functional theory are derived. Finally, different types of basis functions and exchange-correlation potentials used when implementing DFT are presented. Chapter 2.1, 2.2, 2.3, and 2.5 are taken (with some modifications) from the specialization project written by the author in the fall of 2020.

2.1 Quantum Computing

The idea of quantum computing (QC) was first developed in the 1980s by Feynman[17] and Deutsch[18]. This section presents the basic theory behind quantum computing. There are different models of quantum computing, and the one studied here is the quantum circuit model[19], which is most widely used. The main reference for this section is Ref. [19].

2.1.1 Quantum Bits

In classical computers, bits physically represent a transistor state, taking on a value of either 0 or 1. Bits form the memory of classical computers. For quantum computers, the memory stored as a bit is replaced by memory stored as a two-level quantum system. The two-level system is called a quantum bit. A quantum bit (qubit for short) can be described as a mathematical object with certain properties.

Although qubits can be realized as physical objects, here, we first describe them as mathematical objects. In Section 2.1.3, requirements for physical realizations are discussed.

A qubit has two possible states, $|0\rangle$ and $|1\rangle$, but can also be in a state, $|\psi\rangle$, which is a linear combination of the two states $|0\rangle$ and $|1\rangle$,

$$|\psi\rangle = \alpha |0\rangle + \beta |1\rangle, \quad (2.1)$$

where $\alpha, \beta \in \mathbb{C}$. I.e., the qubit is a quantum state vector in a two-dimensional Hilbert space[20]. When measuring a qubit, we get the result 0 or 1. We get 0 with a probability of $|\alpha|^2$ and 1 with a probability of $|\beta|^2$. Also, by normalization, we must have

$$|\alpha|^2 + |\beta|^2 = 1. \quad (2.2)$$

Thus, we can view a qubit as a unit vector in a two-dimensional complex vector space. $|0\rangle$ and $|1\rangle$ are called computational basis states, and they form an orthonormal basis for the vector space.

The qubit can exist in a continuum of states between $|0\rangle$ and $|1\rangle$, but when a measurement is made, this changes the qubit's state. The state will go from a superposition of $|0\rangle$ and $|1\rangle$ to the state corresponding with the measurement result. If the qubit is measured, and the result is 1, then the qubit will be in the state $|\psi\rangle = |1\rangle$. If the result is 0, the qubit will be in the state $|\psi\rangle = |0\rangle$.

The single-qubit state can, in principle, store an infinite amount of information, but a measurement gives 0 or 1 as a result. Therefore, a single measurement will only give a single bit of information about the state. An infinite amount of measurements must be made to determine α and β given in Equation (2.1).

We may also study two-qubit systems, i.e., a system consisting of two qubits. The computational basis of the two-qubit states are constructed from tensor products of the computational basis of the single-qubit system, $\{|0\rangle, |1\rangle\}$, by Postulate 4 of quantum mechanics[19]. I.e., for the two-qubit system, the state is

$$|\psi\rangle = |\psi_1\rangle \otimes |\psi_2\rangle, \quad (2.3)$$

where $|\psi_1\rangle$ is the state of qubit 1, and $|\psi_2\rangle$ is the state of qubit 2. Knowing that the computational basis for both qubit 1 and 2 is $\{|0\rangle, |1\rangle\}$, the computational basis for

the two-qubit system is $\{|0\rangle \otimes |0\rangle, |0\rangle \otimes |1\rangle, |1\rangle \otimes |0\rangle, |1\rangle \otimes |1\rangle\}$. Using the short-hand notation $|m\rangle \otimes |n\rangle \equiv |m\rangle |n\rangle \equiv |mn\rangle$, gives the computational basis $\{00, 01, 10, 11\}$.

We may therefore write the two-qubit state as

$$|\psi\rangle = \alpha_{00} |00\rangle + \alpha_{01} |01\rangle + \alpha_{10} |10\rangle + \alpha_{11} |11\rangle, \quad (2.4)$$

where $\alpha_{00}, \alpha_{01}, \alpha_{10}, \alpha_{11} \in \mathbb{C}$.

A common way of visualizing the state of a single qubit is the Bloch sphere, which is based on rewriting Equation (2.1) as

$$|\psi\rangle = e^{i\gamma} \left(\cos \frac{\theta}{2} |0\rangle + e^{i\phi} \sin \frac{\theta}{2} |1\rangle \right), \quad (2.5)$$

where $\theta, \phi, \gamma \in \mathbb{R}$, and ignoring the global phase factor, $\exp(i\gamma)$, so that the qubit state is described by

$$|\psi\rangle = \cos \frac{\theta}{2} |0\rangle + e^{i\phi} \sin \frac{\theta}{2} |1\rangle. \quad (2.6)$$

By drawing a sphere, where the poles represent the basis states, the state $|\psi\rangle$ can be visualized as shown in Figure 2.1. This is especially useful when we are dealing with transformations of the state, as it gives an intuitive way of visualizing the process.

There is a distinction between the physical and logical qubit. The physical qubit is a physical device that is a two-level quantum system used as a component in the quantum computer. A logical qubit performs as specified in a quantum circuit and has long enough coherence time to be usable by quantum gates. For example, a single logical qubit can be physically realized as six physical qubits.

2.1.2 Quantum Circuits

We describe a qubit by its state. To do computations with a qubit, there needs to be a way of manipulating or changing the qubit's state. Analogous to how a classical *gate* can change a bit from, e.g., 0 to 1, we use *quantum gates* to change a qubit's state. The quantum gates can be connected to form a *quantum circuit*.

By Postulate 2 of quantum mechanics[19], the evolution of a closed quantum system, and therefore a many- or single-qubit state, can be described by a unitary transformation, U , of the initial state. The system $|\psi_i\rangle$ at a time t_i is related to the system $|\psi_f\rangle$ at a time t_f by a unitary operator U ,

$$|\psi_f\rangle = U |\psi_i\rangle. \quad (2.7)$$

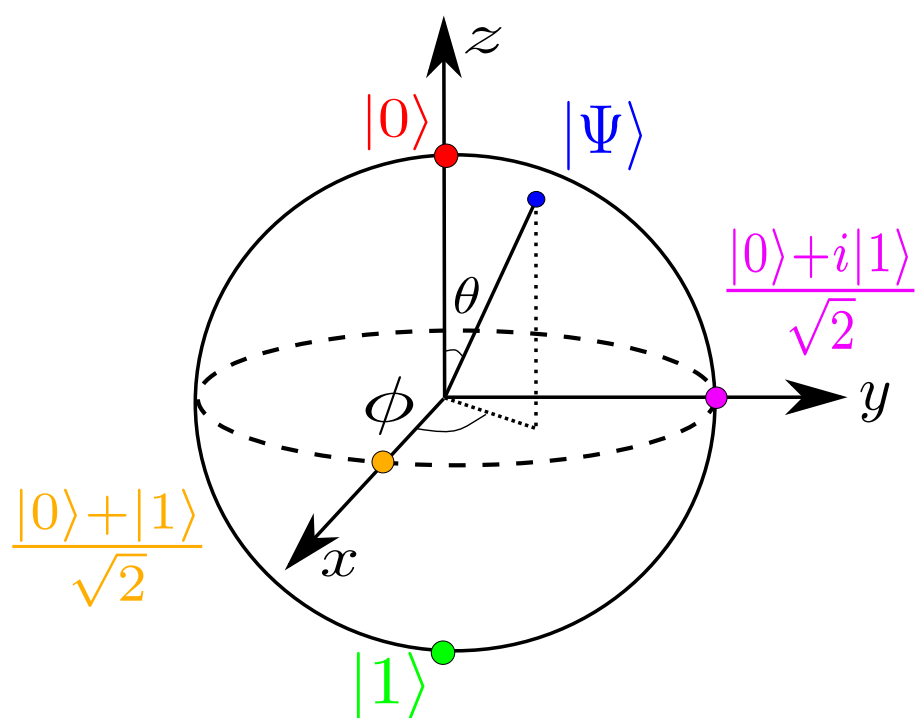


Figure 2.1: Visualization of an arbitrary quantum state of a two-level qubit, $|\Psi\rangle$, on a so-called Bloch sphere. By convention the z -axis is defined as the quantization axis of the Hamiltonian. The position of the $|0\rangle$, $|1\rangle$, $(|0\rangle + i|1\rangle)/\sqrt{2}$ and $(|0\rangle + |1\rangle)/\sqrt{2}$ states on the Bloch sphere are also shown.

The requirement for U to be unitary, i.e., $U^\dagger U = I$, can be understood from the normalization condition. This constraint is also the only constraint for quantum gates.

Here we will look at one- and two-qubit gates only. The basic example of a one-qubit gate is analogous to the classical NOT gate and is called the quantum NOT gate. The gate takes the state $|0\rangle$ to the state $|1\rangle$ and vice versa, by letting the new state after the gate is "applied" be

$$|\psi_f\rangle = \beta|0\rangle + \alpha|1\rangle, \quad (2.8)$$

where the original state was that of Equation (2.1). Observe that this transformation corresponds to acting on the original state with a unitary operator U_{NOT} defined by

$$U_{\text{NOT}} = \begin{pmatrix} 0 & 1 \\ 1 & 0 \end{pmatrix}. \quad (2.9)$$

Unlike in the classical case, as there are infinitely many unitary two by two matrices, there are infinitely many single-qubit quantum gates. Another single-qubit gate is the rotation,

$$R_n(\theta) = \exp\left[-\frac{i\theta\hat{n}\cdot\boldsymbol{\sigma}}{2}\right], \quad (2.10)$$

where \hat{n} is a three-dimensional vector specifying the axis of rotation, θ is the angle of the rotation, and $\boldsymbol{\sigma} = \sigma_x\hat{x} + \sigma_y\hat{y} + \sigma_z\hat{z}$ is a vector of Pauli Matrices[21]. For simplicity we define $X = R_x(90)$, $Y = R_y(90)$ and $Z = R_z(90)$. In addition, $\bar{X} = R_x(-90)$ and $X^2 = R_x(180)$ (and likewise for Y and Z). Some specific examples of the rotation gates are the Hadamard gate,

$$H = \frac{1}{\sqrt{2}} \begin{pmatrix} 1 & 1 \\ 1 & -1 \end{pmatrix}, \quad (2.11)$$

the phase gate,

$$S = \begin{pmatrix} 1 & 0 \\ 0 & i \end{pmatrix}, \quad (2.12)$$

and the $\pi/8$ gate

$$T = \begin{pmatrix} 1 & 0 \\ 0 & \exp(i\pi/8) \end{pmatrix}. \quad (2.13)$$

According to Bloch's Theorem[21], for *any* single-qubit transformation, U , there exist numbers $\alpha, \beta, \gamma, \delta \in \mathbb{R}$, such that

$$U = \exp(i\alpha)R_x(\beta)R_y(\gamma)R_x(\delta). \quad (2.14)$$

I.e., to implement any possible single-qubit transformation, there only needs to be implemented a rotation in the \hat{x} plane and the \hat{y} plane.

A simple two-qubit quantum gate is the controlled-NOT, or CNOT, gate. This gate operates on a two-qubit state, i.e., it has two input qubits. If we have a state on the form $|mn\rangle$, the first qubit, in the state $|m\rangle$, is known as the control qubit, while the second qubit, in the state $|n\rangle$, is known as the target qubit. The action the gate performs is $|m, n\rangle \rightarrow |m, n \oplus m\rangle$, i.e., if the control qubit is set to $|0\rangle$, nothing happens to the target qubit, but if the control is $|1\rangle$, the target is transformed as in the quantum NOT gate. This can be written in matrix form as

$$U_{\text{CNOT}} = \begin{pmatrix} 1 & 0 & 0 & 0 \\ 0 & 1 & 0 & 0 \\ 0 & 0 & 0 & 1 \\ 0 & 0 & 1 & 0 \end{pmatrix}. \quad (2.15)$$

Another two-qubit gate which is often encountered is the *SWAP* gate,

$$SWAP = \begin{pmatrix} 1 & 0 & 0 & 0 \\ 0 & 0 & 1 & 0 \\ 0 & 1 & 0 & 0 \\ 0 & 0 & 0 & 1 \end{pmatrix}. \quad (2.16)$$

which swaps two qubits. The square root of this gate, \sqrt{SWAP} is

$$\sqrt{SWAP} = \begin{pmatrix} 1 & 0 & 0 & 0 \\ 0 & \frac{1}{2}(1+i) & \frac{1}{2}(1-i) & 0 \\ 0 & \frac{1}{2}(1-i) & \frac{1}{2}(1+i) & 0 \\ 0 & 0 & 0 & 1 \end{pmatrix}. \quad (2.17)$$

In classical gates, the NAND gate is universal, meaning that any classical circuit can be built from a specific combination of NAND gates[22]. In quantum computation, there are sets of universal gates, meaning that the set of gates together can form any quantum circuit. It may be shown[19] that one set of universal quantum

gates are the Hadamard, phase, CNOT, and $\pi/8$ gate. As the Hadamard, phase, and $\pi/8$ gates are specific cases of the rotation gate, in principle, only the CNOT and rotation $R_{\hat{n}}(\theta)$ gates need to be implemented. The \sqrt{SWAP} can be created using only CNOT gates, so the \sqrt{SWAP} can be implemented instead of the CNOT gate[23].

A *quantum algorithm* is a sequence of unitary transformations on one or many qubits, but typically not on more than three[11]. I.e., it is implemented by a quantum circuit. If a quantum computer can implement the CNOT and rotation $R_{\hat{n}}(\theta)$ gates, any quantum algorithm is in principle possible to implement. Quantum algorithms that are known to be faster than the best known classical algorithms are the quantum Fourier transform[24] and quantum search algorithms[25].

2.1.3 Physical Realization of Quantum Computers

Having studied the theoretical basis for quantum computers, we now discuss how they can be physically implemented. We defined a qubit mathematically as a quantum two-level system, i.e., it is in the state $|\psi\rangle = \alpha|0\rangle + \beta|1\rangle$, but we have not stated *what kind of physical system* that can be used to represent a qubit. Thus, a major part of realizing a quantum computer is determining what physical system should represent the qubit. One requirement is that it must be a two-level quantum system. Some examples of quantum two-level systems are the ground state and excited states of an atom and the two spin states of a spin-1/2 particle (e.g., the electron). In addition to simply representing the qubit, the system selected must also allow the qubit to evolve as desired, e.g., by applying unitary transformations. Also, one must be able to prepare the qubits in an initial state and measure the qubits' final state. Note that the requirement that the qubit needs to be allowed to evolve and be measured is opposing. For the qubit to keep its quantum properties, there cannot be significant coupling with the environment, as this will cause decoherence. However, to evolve the system as desired, there needs to be some coupling with the environment.

Five basic requirements must be satisfied for the physical implementation of a quantum computer. These are often called "DiVincenzo's requirements", as proposed in 2000 by David P. DiVincenzo[11]. The criteria are stated below by DiVin-

cenzo's definition. There are also two requirements related to quantum communication, which will not be discussed here.

Requirement 1: "A scalable physical system with well-characterized qubits"

To have a quantum computer, there needs to be a *physical system*, which contains several qubits. DiVincenzo states that the qubit needs to be "well-characterized", by which he means that the properties of the system in which the qubits are encoded must be known (e.g., the spin of the electron), including the internal Hamiltonian (which includes any coupling with other states, interactions with other qubits, and coupling to external fields)[11].

Requirement 2: "The ability to initialize the state of the qubits to a simple fiducial state, such as $|000\dots\rangle$ "

The initial state needs to be known, but there needs to be a continuous supply of a *low-entropy* state for quantum error correction. The two main approaches for initializing the starting state are by cooling or by a measurement that projects the system into a state (or rotates into the desired state).

Requirement 3: "Long relevant decoherence times, much longer than the gate operation time"

Decoherence is the process in which the qubit state couples with the environment, losing its original state. Quantum error correction can be successful if the decoherence time is $10^4 - 10^5$ times the time it takes to execute an individual quantum gate.

Requirement 4: "A "universal" set of quantum gates"

Any wanted quantum gate should be possible to implement in the physical realization. As explained in Section 2.1.2, the CNOT and the rotation gate $R_{\hat{n}}(\theta)$ can be used to implement all possible quantum gates and these will represent the minimum of gates that need to be implemented. We do not expect these to be implemented perfectly, but this error is another decoherence source that must be dealt with in quantum error-correcting algorithms. The magnitude of random errors should be

$10^{-4} - 10^{-5}$ per gate operation for it to be tolerable.

Requirement 5: "A qubit-specific measurement capability"

After the computation is complete, there needs to be a way to measure the result of specific qubits, which is called readout. A measurement that is very close to the actual state of the qubit is said to have high fidelity[19]. Ideally, the fidelity should be 100%, but much less is needed for quantum computation. If higher reliability is required, the calculation can run multiple times.

It is not realistic or necessary that all of these requirements are completely satisfied for a functioning quantum computer system. To evaluate to what degree these requirements are satisfied, several quantities have been defined to compare different physical implementations. These quantities are important for evaluation, and have become conventional to compute in quantum computing experiments: T_1 , T_2 , T_2^* and gate/readout fidelity.

First, we note that Requirement 3 states that the decoherence times must be long. Two measurements that encapsulate the decoherence are the energy relaxation time, T_1 , and the coherence time, T_2 . Other names are also used in literature for these times, but the symbols used, T_1 and T_2 , indicate the meaning. Due to energy exchange with the environment, a qubit out of equilibrium will return to thermal equilibrium. T_1 is the time constant of the equilibrium process and can be determined experimentally via inversion recovery and saturation recovery. For times larger than T_1 , the qubit's superposition state will end up in the ground state, and coherence is lost. T_2 is a time that indicates how long a qubit can remain *phase coherent*. Other terms often used are dephasing time, transverse relaxation time, and phase randomization time. At times larger than T_2 , the evolution around the Bloch sphere (Figure 2.1) is lost track of, and we can no longer control it. T_2 is an important metric for a system, as it indicates how many operations can be completed on the computer. T_2 is commonly also called Hahn Echo time due to the experiment commonly used to measure this quantity. Another measurement commonly used is the Ramsey experiment time (or Ramsey time), T_2^* . The name comes from the experiment used to find this characteristic time. Note that T_2^* is

also called decoherence time or dephasing time.

There needs to be a way to quantify how good a readout is due to Requirement 4. A commonly used quantity is fidelity,

$$F(|\psi\rangle, |\phi\rangle) = |\langle\phi|\psi\rangle|, \quad (2.18)$$

where $|\phi\rangle$ and $|\psi\rangle$ are two pure states, such that if the two states are equal, the fidelity is 1[21]. Often in literature, the fidelity is stated in percentages so that 100% corresponds to a fidelity of 1. Fidelity can also be used to evaluate the control precision of a quantum gate (gate fidelity). In practice, readout fidelities of above 99% has been achieved[26].

2.2 Electron Spin Qubits

In this section, the physical implementation of qubits as the two-level electron spin confined in a quantum dot (QD) is studied. The main references for this section are Ref. [20] and Ref. [23].

2.2.1 Quantum Dots

A quantum dot is a semiconductor that can be filled with electrons or holes. In this project, only QDs filled with electrons will be discussed. The QD can be coupled via tunnel barriers to reservoirs in which electrons can be exchanged. The current and voltage of these reservoirs can be controlled and measured. The QD is also coupled capacitively to one or more gate electrodes, which is used to set the electrostatic potential w.r.t. the electron reservoirs. The definition of a QD is very general, and there are many different types of QDs, varying in, e.g., size, material, and production method. A schematic visualization of a possible quantum dot setup is shown in Figure 2.2.

Two effects influence the electrical properties of QDs. The first effect is that due to the potential, the electron is confined in all three directions to the QD. Also, Coulomb repulsion between electrons requires energy for another electron to enter the QD. At low temperatures, the repulsion can lead to electrons not being able to tunnel into the QD, which effectively blocks electrons out from the QD. This is

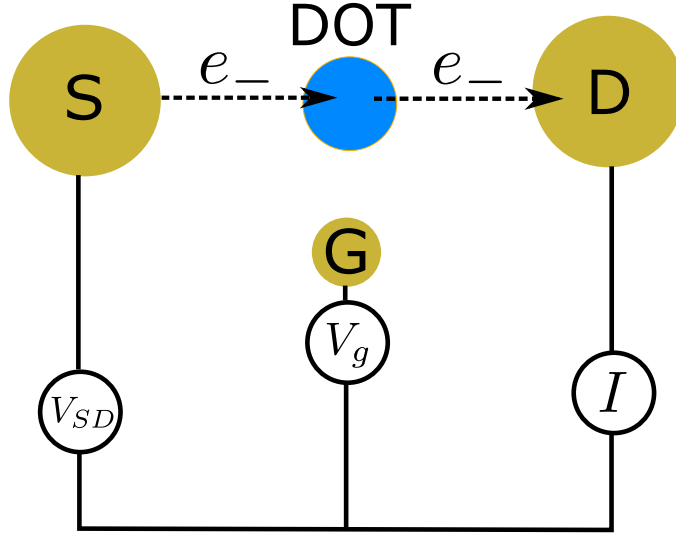


Figure 2.2: Schematic figure of a lateral quantum dot structure. S is the source, D is the drain, and G is the gate (in yellow). V_{SD} is the bias voltage, and V_g is the voltage applied to the gate. I is the current through the device and is measured in response to the bias voltage and the gate voltage. The dot (here in blue) consists of one or more electrons confined due to the applied potential at the gate. Electrons may, under certain conditions, tunnel onto the dot from the source and off the dot to the drain, which will give a current through the structure.

known as Coulomb blockade and is important in certain methods for read-out of the qubit state after spin manipulation.

2.2.2 Spin States in a Single Quantum Dot

A possible physical implementation of a qubit is the spin of a single electron. The electron has a spin of $1/2$, and the z -component of the spin takes one of the two possible values $\pm\hbar/2$ [20]. The operator of the z -component of the spin is

$$s_z = \frac{\hbar}{2} \begin{pmatrix} 1 & 0 \\ 0 & -1 \end{pmatrix} = \frac{\hbar}{2} \sigma_z, \quad (2.19)$$

where σ_z is the z Pauli matrix. It is conventional to let the spin-up state, i.e., with positive spin, be the $|0\rangle$ state, and the spin-down state, i.e., with negative spin, be the $|1\rangle$ state, so that $|0\rangle$ and $|1\rangle$ states can be written as

$$|0\rangle = |\uparrow\rangle = \begin{pmatrix} 1 \\ 0 \end{pmatrix}, |1\rangle = |\downarrow\rangle = \begin{pmatrix} 0 \\ 1 \end{pmatrix}. \quad (2.20)$$

The spin has an associated magnetic moment,

$$\mu_s = -\frac{1}{2}g\mu_B\sigma_z, \quad (2.21)$$

where g is the effective Lande factor, σ_z is the z Pauli matrix and μ_B is the Bohr magneton, which has the value $\mu_B = 0.927 \cdot 10^{-23} \text{ Am}^2$. For an electron in vacuum, $g = 2.0$, but in materials, it can take both positive and negative values. In Si, the value of the Lande factor is $g = 1.998$ [20]. The spin's magnetic moment will couple with an external magnetic field, \mathbf{B} . Letting $\mathbf{B} = B_0\hat{z}$, the Hamiltonian is given by

$$H = -\mu_s B_0 = \frac{1}{2}g\mu_B\sigma_z B_0. \quad (2.22)$$

The eigenvalues of H are the energy levels of the system,

$$E_{\pm} = E_0 \pm \frac{1}{2}g\mu_B B_0, \quad (2.23)$$

which experience *splitting*, called Zeeman splitting. I.e., the energy of the system with spin-down is different than with spin-up. This will be of significance when developing methods for physically implementing the unitary transformations (i.e., quantum gates) of the system.

It may also be beneficial to form the qubit from *two* electron spins in a single QD. In this case, the two electrons together form the (approximately) isolated system, and are coupled. At zero magnetic field the ground state of the spin in this system is when the electrons have opposite spin[23],

$$|\psi\rangle = \frac{1}{\sqrt{2}}(|\uparrow\downarrow\rangle - |\downarrow\uparrow\rangle). \quad (2.24)$$

The total spin is zero, $S = 0$, and the state is called a *spin singlet*. The lowest-energy excited states (again in zero magnetic field) are the degenerate *spin triplets*,

$$|T_+\rangle = |\uparrow\uparrow\rangle, |T_0\rangle = \frac{1}{\sqrt{2}}(|\uparrow\downarrow\rangle + |\downarrow\uparrow\rangle), |T_-\rangle = |\downarrow\downarrow\rangle. \quad (2.25)$$

The singlet and triplet states are visualized in Figure 2.3.

Due to the Pauli principle, one of the electrons in the triplet state has to occupy a higher energy orbital. Although $S = 1$, the z -component of the spin-states differ, and they are $S_z = 1$, $S_z = 0$ and $S_z = -1$, respectively. In the same way as for a single electron QD, an applied magnetic field, \mathbf{B} , leads to splitting in the energy levels of the triplets (Zeeman splitting).

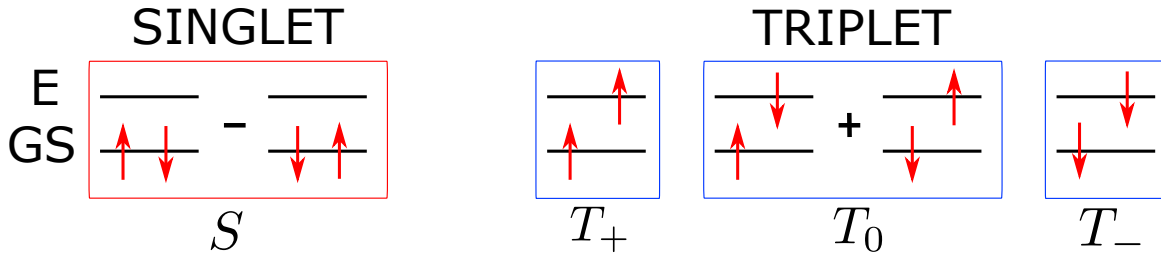


Figure 2.3: Visualization of the spins of the singlet and triplet states, with the energy levels shown. E is the first excited state, and GS is the ground state. S shows the spin-singlet, and T_+ , T_0 and T_- are the spin-triplet. E.g., for the triplet T_+ , both spins have spin-up, but one is in the ground state, while the other is in the first excited state.

2.3 Control Techniques

Nuclear magnetic resonance (NMR) was developed as a protein structure determination tool, where thousands of complicated and precise pulses are applied to molecules that contain hundreds of spins[21]. Closely related to NMR is electron spin resonance (ESR). ESR is based on the same theory and technique but, as the name suggests, is based on the spin of the electron rather than the spin of the atomic nuclei. ESR uses magnetic fields, while yet another method, electric-dipole spin resonance (EDSR), uses a different mechanism.

In Section 2.2 we looked at how we could realize a qubit from the spin of the electron. To control the electron spin, i.e., apply the quantum gates through unitary transformations, there needs to be a way of *manipulating* the spin state. One possible way (although many other approaches exist) of controlling the spin-state is through ESR and EDSR. In this section, the theory behind ESR is discussed. The main reference for this section is Ref. [21].

2.3.1 Electron Spin Resonance

To describe the quantum system together with the electromagnetic pulse controlling the system, we may split the Hamiltonian into two parts,

$$H = H_{\text{sys}} + H_{\text{control}}, \quad (2.26)$$

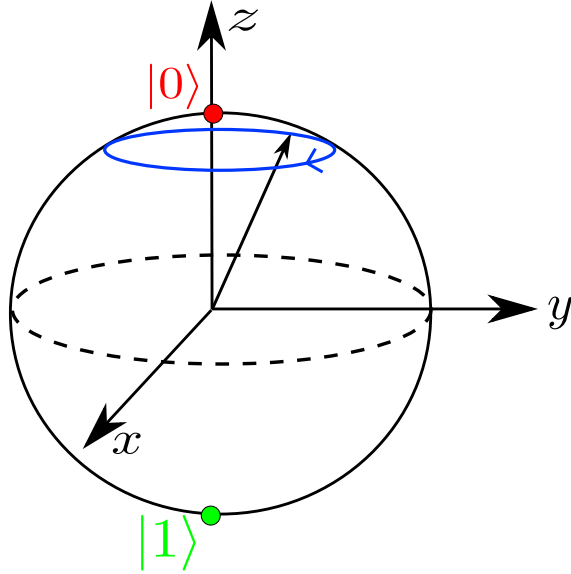


Figure 2.4: Visualization on a Bloch sphere of the precession of the state vector about $\mathbf{B}_0 = B_0 \hat{z}$.

where H_{sys} is the Hamiltonian without any control, i.e., the quantum dot qubit system, and H_{control} is the Hamiltonian of the terms that are under external control[21]. In ESR H_{control} arises from sequences of pulses of electromagnetic radiation.

As discussed in Section 2.2.2, the Hamiltonian of a spin which is coupled to a magnetic field, $\mathbf{B} = B_0 \hat{z}$ is

$$H_0 = \frac{1}{2} g \mu_B \sigma_z B_0. \quad (2.27)$$

The state vector will precess around the magnetic field vector, visualized on the Bloch sphere in Figure 2.4.

The mechanics of which the ESR system is controlled are through applying an electromagnetic field, $\mathbf{B}_1(t)$, which rotates in the $\hat{x} - \hat{y}$ plane at frequency ω_{rf} [21], in addition to the static field, B_0 . The rotating field is conventionally called the radio-frequency (RF) field. When $\hbar \omega_{rf} = g \mu_B B_0$, the spin will be coherently rotated up and down.

To create the RF field experimentally, a magnetic field oscillated along a fixed axis perpendicular to the B_0 -field is applied. Then the field is decomposed into two fields that rotate in opposite directions. One field rotates at frequency ω_{rf} in the same direction as the spin rotates. The other field rotates in the other direction and is far from resonance, such that the shift in the Larmor frequency (the Bloch-Siegert shift) is negligible[21]. Controlling the RF field is what will enable us to

control quantum systems by ESR.

The RF field has almost no effect on far off-resonance spins. In this way, any one qubit can be selectively rotated without rotating any of the other spins. Spins with Larmor frequency closer to RF rotate somewhat, but a single pulse cannot flip the spin.

2.3.2 Electron Spin Resonance for Manipulation of Spin States

The principle of ESR is that a rotating magnetic field, B_1 is applied perpendicularly to the static field B_0 (i.e., the field which causes the Zeeman splitting), which is along \hat{z} . B_1 is on-resonance with the energy difference ΔE , i.e., the energy needed to flip a spin. To use ESR for control of electron spin-based qubits, the needed unitary transformations, U , need to be implemented. The transformation, U , is specified in terms of a sequence $U = U_k U_{k-1} \dots U_2 U_1$, where U_i are standard quantum gates. As discussed in Section 2.1.2, only the CNOT and rotation ($R_{\hat{n}}(\theta)$) gates need, in principle, to be implemented to be able to implement any quantum algorithm.

Rotation gates, $R_{\hat{n}}(\theta)$, can be implemented using RF pulses. When an RF field of amplitude ω_1 is applied to a single-spin system at frequency $\omega_{rf} = \omega_0$, the spin evolves under the transformation (in the rotation frame)

$$U = \exp[i\omega_1(\cos \phi I_x + \sin \phi I_y)t_{pw}], \quad (2.28)$$

where t_{pw} is called the pulse width, which is the duration of the RF pulse. U describes a rotation over an angle θ proportional to the product of t_{pw} and $\omega_1 = \gamma B_1$, about an axis in the $\hat{x} - \hat{y}$ plane determined by ϕ . Thus rotations can be implemented by changing the phase, ϕ , or the product $\omega_1 t_{pw}$. Note that only the relative phase between pulses applied to the same spin matters. The absolute phase does not matter itself but establishes a reference against which the subsequent pulses should be compared.

The CNOT gate is a two-qubit gate, i.e., two-qubit states are transformed. The gate can be implemented by turning on an exchange interaction, which leads to an ESR transition. The transition can be implemented with a microwave pulse. Two

nearby spins are coupled by a Hamiltonian on the form

$$H_e(t) = J(t)\mathbf{S}_1 \cdot \mathbf{S}_2. \quad (2.29)$$

where $J(t)$ is the time-dependent exchange constant, produced by turning on and off the tunneling matrix element $t_0(t)$ and u is the charging energy of a single dot[5].

The time evolution operator is $U_J(t) = \exp(-iJS_1S_2t)$. Letting the evolution occur for a time $t = 1/(2J)$, gives the controlled phase up gate, up to a 90-degree phase shift on each qubit, and an overall phase[21],

$$U_{CPHASE} = \sqrt{-i}\bar{Z}_1\bar{Z}_2U_J(1/2J) \quad (2.30)$$

where the subscript of the operators denotes which qubit it is operating on and $\bar{Z} = R_z(-90)$ (as defined in Section 2.1). Control of J can be used to implement a CNOT gate, as the CPHASE gate is equivalent to the CNOT gate to a basis change of the target qubit and a phase shift on the control qubit[21], so that

$$\begin{aligned} U_{CNOT} &= iZ_1^2\bar{Y}_2U_{CPHASE}Y_2 \\ &= \sqrt{i}Z_1\bar{Z}_2X_2U_J(1/2J)Y_2 \\ &= \begin{pmatrix} 1 & 0 & 0 & 0 \\ 0 & 1 & 0 & 0 \\ 0 & 0 & 0 & 1 \\ 0 & 0 & 1 & 0 \end{pmatrix}. \end{aligned} \quad (2.31)$$

2.3.3 EDSR for Qubit Control

ESR has disadvantages due to heating and large coils or magnets needed. An alternative is electric-dipole spin resonance. One way of doing EDSR is with spin-orbit interaction (SOI) or an inhomogeneous magnetic field. The magnetic field couples the electric field to the electron spin (not directly to the spin states as in ESR). Another possibility is to use the hyperfine interaction and g -tensor modulation resonance. Golovach *et al.*[27] showed that there are two major mechanisms of EDSR in QDs. One from the linear momentum in the Dresselhaus and Rashba SOI combined with the Zeeman interaction, and the other from the cubic Dresselhaus terms in combination with the cyclotron frequency[27].

The spin-orbit interaction can be used by setting up a static magnetic field \mathbf{B}_z and an ac electric field $\mathbf{E}(t)$ to control the spin. EDSR will couple *orbital states* to spin states, with SOI working as a mediator. The effective Hamiltonian is given by[27]

$$H = H_{dot} + H_z + H_{SOI}, \quad (2.32)$$

where

$$H_z = \frac{1}{2}g\mu_B\mathbf{B}_z \cdot \boldsymbol{\sigma}, \quad (2.33)$$

is the Zeeman splitting and

$$H_{SOI} = \frac{1}{2}g\mu_B\mathbf{B}_{\text{eff}} \cdot \boldsymbol{\sigma}, \quad (2.34)$$

is the SOI Hamiltonian. Here μ_B is the Bohr magneton, \mathbf{B}_z is the static magnetic field, \mathbf{B}_{eff} is the effective SOI driving field which is caused by the electric field, and $\boldsymbol{\sigma}$ is the Pauli matrix vector.

If assuming that the static field and electric field is along the [110] or $[\bar{1}\bar{1}0]$ plane of the crystal structure, B_{eff} can be written as

$$|B_{\text{eff}}| = 2|B_z|\frac{eE(t)l_{dot}^2}{l_{SO}\Delta}, \quad (2.35)$$

where l_{SO} is the spin-orbit length defined as

$$l_{SO} = \frac{\hbar}{m^*(\alpha + \beta)}, \quad (2.36)$$

where l_{dot} is the physical size of the dot, Δ is the orbital energy splitting, and m^* is the effective mass. α and β are the Rashba and Dresselhaus spin-orbit coefficients. The speed of the EDSR manipulation depends on Δ , and can be seen as the shift of the center of the electron wave function in the dot, $\Delta x = (eE(t)l_{dot}^2)/\Delta$.

Another way is by applying an inhomogeneous magnetic field[28]. If instead a static magnetic field B_0 is applied in the x -direction, and applying an inhomogeneous field, written as

$$B_{sl}(x) = b_{sl}xz, \quad (2.37)$$

where b_{sl} is the z -direction gradient of the field parallel to the x -axis (slanting field). The middle of the QD is taken to be at $z = 0$. The effective shift of the center, Δx due to the ac electric field, leads to an effective alternating magnetic field,

$$B_{\text{eff}}(t) = -b_{sl}\frac{eE(t)l_{dot}^2}{\Delta}z. \quad (2.38)$$

In practice, this is often implemented by an on-chip micro-magnet, e.g., made of cobalt[28].

2.4 Solid State Physics

The main reference for this section is Ref. [29]. Only the definitions and explanations needed directly for the thesis will be presented here. For a further introduction, see, e.g., the book by Kittel[29].

An ideal crystal can be described as a set of atoms with discrete translational symmetry, where the atoms are periodically infinitely repeated in space. Three translation vectors (in three dimensions) can be defined as a_1 , a_2 and a_3 . The unit cell is the smallest possible cell that can be constructed, which, when repeated, constructs the crystal. In three dimensions, three lattice constants a , b , and c can be defined, which describe the distance between unit cells.

There are only a limited number of possible unit cell types. One common type is the face-centered cubic (fcc) cell, which consists of lattice points in a cube in addition to lattice points on the faces (center of side) of the cube, giving $a = b = c$. The unit cell can be constructed by four lattice points, with a single atom basis located at the origin, defined by three vectors

$$\mathbf{a}_1 = \left(\frac{a}{2}, \frac{a}{2}, 0\right), \quad \mathbf{a}_2 = \left(\frac{a}{2}, 0, \frac{a}{2}\right), \quad \mathbf{a}_3 = \left(0, \frac{a}{2}, \frac{a}{2}\right). \quad (2.39)$$

With two identical atoms in the basis, positioned at $(0, 0, 0)$ and $(a/2, a/2, a/2)$, the fcc lattice is called a diamond cubic lattice. The volume of a unit cell is $V = |\mathbf{a}_1 \cdot \mathbf{a}_2 \times \mathbf{a}_3|$, which for an fcc cell is $V_{\text{fcc}} = a^3/4$.

It is often convenient to describe the properties of the crystal system through its Fourier transform, called reciprocal space or k -space. The reciprocal lattice is described in k -space by the reciprocal lattice vectors

$$\mathbf{b}_1 = 2\pi \frac{\mathbf{a}_2 \times \mathbf{a}_3}{\mathbf{a}_1 \cdot \mathbf{a}_2 \times \mathbf{a}_3}, \quad \mathbf{b}_2 = 2\pi \frac{\mathbf{a}_3 \times \mathbf{a}_1}{\mathbf{a}_1 \cdot \mathbf{a}_2 \times \mathbf{a}_3}, \quad \mathbf{b}_3 = 2\pi \frac{\mathbf{a}_1 \times \mathbf{a}_2}{\mathbf{a}_1 \cdot \mathbf{a}_2 \times \mathbf{a}_3}. \quad (2.40)$$

A translational invariant vector in k -space is $\mathbf{G} = m_1 \mathbf{b}_1 + m_2 \mathbf{b}_2 + m_3 \mathbf{b}_3$, with m_i being integers.

An important definition with relation to k -space is the Brillouin zone (BZ). The BZ is defined as all points in k -space closer to the origin than any other points. The

first BZ (1BZ) is defined as $-\pi/2 \leq k \leq \pi/2$, where a is the lattice constant in all directions and k is the size of the wave vector. The 1BZ contains all information about the structure, due to the structure being translationally invariant, so that all information outside of the 1BZ can be found by translating by $n\mathbf{G}$ (n being an integer). For a diamond structured lattice, the reciprocal lattice vectors are found to be

$$\mathbf{b}_1 = 2\pi/a(-1, 1, 1), \mathbf{b}_2 = 2\pi/a(1, -1, 1), \mathbf{b}_3 = 2\pi/a(1, 1, -1). \quad (2.41)$$

The point group has 48 symmetry elements, reflected in the symmetry of the 1BZ. There are certain points within and on the 1BZ which are high symmetry and of interest. The Γ point is at the center of the 1BZ, i.e., $\mathbf{k} = (0, 0, 0)$. The X points are at the edge of the 1BZ in the 100 directions (i.e., the middle of one of the squares of the 1BZ). Points that lie between Γ and X are denoted by the Δ direction.

An ideal crystal as defined above is a periodic system, meaning that if the nuclei of the atoms are static the potential can be viewed as a periodic potential. Bloch's theorem states that solutions to the Schrödinger equation in a periodic potential is given by

$$\psi_{\mathbf{k}}(\mathbf{r}) = u_{\mathbf{k}}(\mathbf{r})e^{i\mathbf{k}\cdot\mathbf{r}}, \quad (2.42)$$

where $u_{\mathbf{k}}(\mathbf{r})$ has the periodicity of the crystal lattice, $u_{\mathbf{k}}(\mathbf{r}) = u_{\mathbf{k}}(\mathbf{r} + \mathbf{T})$, which modulates the plane waves.

For a system containing electrons, there are different energy-regions which either are forbidden or allowed energies. The regions of allowed energies are called bands and can be found from the wave functions in the allowed energy regions. For each k , several energy states, n , can exist. In a semiconductor, the conduction band is the lowest-lying forbidden band, and the valence band is the highest lying allowed band. The Fermi energy, E_F , is the energy value of the highest energy electron state.

2.5 Silicon for Quantum Technologies

Natural silicon consists of three stable isotopes, ^{28}Si , ^{29}Si and ^{30}Si [30]. Of these three, only ^{29}Si has a non-zero nuclear spin. The abundance of ^{29}Si is only 4.67%[30]. Due to this low abundance, the hyperfine interaction between spins is small, leading to

very low electronic spin decoherence times[14]. In addition, it is possible to isotopically enrich natural silicon to reduce the effect of the hyperfine interactions[31]. The spin-orbit coupling in silicon is small[32]. Both of these mechanisms make silicon desirable due to the potential for a long decoherence time. Silicon does however have multiple conduction-band minima (valleys at the same energy), which unless lifted, can reduce coherence[33]. In recent years, there has been tremendous progress in the research on silicon-based qubits. Long coherence times have been achieved, as well as two-qubit gates. The next step for silicon-based qubits is large-scale integration. It should be noted that although the overall goal is to make a fault-tolerant QC, this is a rather distant goal, so first a large-scale QC with noisy qubits (i.e., no error correction) should be implemented.

Bulk crystalline silicon is a covalently bonded crystal that has a diamond (face-centered-cubic) lattice structure[29]. Silicon has an indirect band gap, i.e., the energies of the electron states in the conduction band have a minima at $k \neq 0$. At room temperature the band gap is $E_g = 1.12$ eV, and at 4 K it is $E_g = 1.17$ eV[29]. In the valence band, the heavy and light hole bands are degenerate for $k = 0$, and the split-off band is separated from the other sub-bands by the spin-orbit splitting. Bulk Si has cubic symmetry, and there are six equivalent minima, i.e., it has six degenerate valleys[33]. The physics of the valley states play an important role in quantum electronics, like QDs. It can lift Pauli spin blockade, complicating spin control. In addition, a qubit needs to be an effective two-level system, and this should be made of the spin states, not the valley splitting.

In a two-dimensional electron gas, like in a QD, the degeneracy is broken into a two-fold degenerate ground state, Γ valleys, and a four-fold degenerate excited state, Δ valleys. The twofold degeneracy is broken by electronic confinement induced by electric fields and by the quantum well. This breaking of degeneracy is necessary so that the spins, not the valleys, form the two-level system (qubit).

If the orbital level spacing and valley splitting are approximately equal, valley and orbit states can hybridize, giving valley-orbit mixing. Instead of referring to a pure valley splitting E_v , we call it valley-orbit splitting, $E_{VO} = E_{VO2} - E_{VO1}$, where E_{VOi} is the energy of the i th hybridized valley-orbit number (called the ground-state gap)[34].

The behavior of the valley splitting is complicated, as the interfaces are not perfectly smooth and oriented perpendicular to z . The energy difference between the two lowest valley states depends on the relation between the phase of the oscillations of the wave function with the boundary. A *step* in the interface changes the phase relationship. The phase of the oscillations can become dependent on the x and y coordinates. This coupling is called *valley-orbit coupling*. Valley splitting is suppressed if the step density in the well is high, but if an electron is confined to a region small enough that does not extend over multiple steps, the valley splitting is not affected by the step density. At low temperatures, relevant for quantum computing, the splitting is large enough so that valley excitations will not happen. Valley splitting and valley-orbit coupling depend on interface details, so the values of the valley splitting can vary significantly between devices.

Development for silicon-based QDs has generally been behind other semiconductor materials, like GaAs. This is largely due to fabrication and design challenges. Silicon has a large in-plane effective mass, nearly three times larger than in GaAs, which decreases the area of the wave function where the QD is formed[35]. A smaller wave function requires smaller devices to allow for the isolation of a single electron.

2.6 Hyperfine Interactions

In this section, the hyperfine interaction (HFI) parameters for an axially symmetric system are derived from the Dirac equation. The derivation of the Hamiltonian from the Dirac equation is based on Ref. [36]. The derivation of the hyperfine parameters are based on Ref. [37].

2.6.1 Derivation of the Hyperfine Interactions From the Dirac Equation

The Dirac Hamiltonian for an electron in an electromagnetic field with scalar potential ϕ and vector potential \mathbf{A} is given by

$$H = c\boldsymbol{\alpha} \cdot \boldsymbol{\pi} + \beta mc^2 - e\phi, \quad (2.43)$$

where $-e$ is the electron charge, m is the rest mass of the electron, $\boldsymbol{\pi} = \mathbf{p} + e\mathbf{A}$ with \mathbf{p} being the momentum operator, and

$$\alpha_i = \begin{pmatrix} 0 & \sigma_i \\ \sigma_i & 0 \end{pmatrix}, \quad \beta = \begin{pmatrix} \mathbf{1} & 0 \\ 0 & -\mathbf{1} \end{pmatrix} \quad (2.44)$$

are 4×4 Dirac matrices constructed from the Pauli matrices, σ_i . A solution to the eigenvalue equation (Dirac equation), $H\psi = \epsilon\psi$, is a four-component Dirac spinor

$$\psi = \begin{pmatrix} \psi_1 \\ \psi_2 \end{pmatrix}, \quad (2.45)$$

here written as two two-component spinors, ψ_1 and ψ_2 . The Dirac equation can be written as two coupled matrix equations,

$$(\epsilon' + e\phi)\psi_1 - c\boldsymbol{\sigma} \cdot \boldsymbol{\pi}\psi_2 = 0 \quad (2.46)$$

and

$$(\epsilon' + 2mc^2 + e\phi)\psi_2 - c\boldsymbol{\sigma} \cdot \boldsymbol{\pi}\psi_1 = 0, \quad (2.47)$$

with $\epsilon' = \epsilon - mc^2$. Inserting Equation (2.47) into Equation (2.46) by solving for ψ_2 gives ψ_2 in terms of ψ_1

$$\psi_2 = \frac{1}{2mc^2 + e\phi + \epsilon'} \boldsymbol{\sigma} \cdot \boldsymbol{\pi}\psi_1. \quad (2.48)$$

The eigenvalue equation for ψ_1 is

$$\left[\boldsymbol{\sigma} \cdot \boldsymbol{\pi} \frac{c}{2mc^2 + e\phi + \epsilon'} \boldsymbol{\sigma} \cdot \boldsymbol{\pi} - e\phi \right] \psi_1 = \epsilon\psi_1. \quad (2.49)$$

In the non-relativistic regime ψ_1 , called the large component, is much larger than ψ_2 , called the small component. ψ_1 and ψ_2 decouples in the limit

$$\frac{\epsilon' + e\phi}{mc^2} \rightarrow 0, \quad (2.50)$$

so that the small component may be neglected. By introducing the electric field, $\mathbf{E} = -\nabla\phi$, the Hamiltonian can be rewritten (using $(\boldsymbol{\sigma} \cdot \mathbf{O}_1)(\boldsymbol{\sigma} \cdot \mathbf{O}_2) = \mathbf{O}_1 \cdot \mathbf{O}_2 + i\boldsymbol{\sigma} \cdot \mathbf{O}_1 \times \mathbf{O}_2$) as

$$H_1 = \frac{2mc^2}{\epsilon' + 2mc^2 + e\phi} \frac{p^2}{2m} - e\phi + H_c + H_{dip} + H_L + H_{SO} + H', \quad (2.51)$$

where

$$H_c = \frac{e^2 \hbar c^2}{(\epsilon' + 2mc^2 + e\phi)^2} \boldsymbol{\sigma} \cdot \mathbf{E} \times \mathbf{A} \quad (2.52)$$

is called the contact hyperfine interaction,

$$H_{dip} = \frac{e\hbar c^2}{\epsilon' + 2mc^2 + e\phi} \boldsymbol{\sigma} \cdot (\boldsymbol{\nabla} \times \mathbf{A}) \quad (2.53)$$

is the dipolar hyperfine interaction,

$$H_L = \frac{2ec^2}{\epsilon' + 2mc^2 + e\phi} \mathbf{A} \cdot \mathbf{p} \quad (2.54)$$

is the nuclear-orbital interaction,

$$H_{SO} = \frac{\hbar ec^2}{(\epsilon' + 2mc^2 + e\phi)^2} \mathbf{E} \times \mathbf{p} \cdot \boldsymbol{\sigma} \quad (2.55)$$

is the spin-orbit interaction, and H' contains relativistic effects which are independent of the spin of the electron and are neglected.

The contact hyperfine interaction can be further written for a semiconductor nanostructure. For these structures, the electron wave function is generally spread over many of the charged and (possibly) finite-spin nuclei of the underlying material. A nuclear spin with charge Ze and magnetic moment $\boldsymbol{\mu}_I = \gamma \mathbf{I}$ (where γ is the nuclear gyromagnetic ratio and \mathbf{I} is the nuclear-spin operator) will generate electric fields of size¹

$$\phi(\mathbf{r}) = \frac{Ze}{4\pi\epsilon_0 r}, \quad \mathbf{E}(\mathbf{r}) = -\boldsymbol{\nabla}\phi(\mathbf{r}) = \frac{Ze}{4\pi\epsilon_0 r^3} \mathbf{r}, \quad (2.56)$$

and a vector potential

$$\mathbf{A}(\mathbf{r}) = \frac{\mu_0 \gamma \mathbf{I} \times \mathbf{r}}{4\pi r^3}. \quad (2.57)$$

Approximating for a non-relativistic electron with $\epsilon' \ll mc^2$, gives a contact hyperfine interaction of

$$H_c = \mu_0 \mu_B \gamma \delta_T(r) [\boldsymbol{\sigma} \cdot \mathbf{I} - (\boldsymbol{\sigma} \cdot \hat{\mathbf{r}})(\mathbf{I} \cdot \hat{\mathbf{r}})], \quad (2.58)$$

where μ_B is the Bohr magneton, $\hat{\mathbf{r}} = \mathbf{r}/r$, and

$$\delta_T(r) = \frac{1}{4\pi r^2} \frac{r_T/2}{(r + r_T/2)^2}. \quad (2.59)$$

Here

$$r_T = \frac{1}{4\pi\epsilon_0} \frac{Ze^2}{mc^2} \quad (2.60)$$

¹In the following we assume a constant electron g -factor of $g_e = 2$.

is called the Thomson radius, where a_0 is the Bohr radius. Considering the matrix elements of the contact Hamiltonian with respect to two arbitrary states $|a\rangle$ and $|b\rangle$,

$$\langle a|H_c|b\rangle = \mu_0\mu_B\gamma \int d\mathbf{r} \delta_T(r) \psi_a^*(\mathbf{r}) [\boldsymbol{\sigma} \cdot \mathbf{I} - (\boldsymbol{\sigma} \cdot \hat{\mathbf{r}})(\mathbf{I} \cdot \hat{\mathbf{r}})] \psi_b(\mathbf{r}), \quad (2.61)$$

where $\psi_a(\mathbf{r}) = \langle r|a\rangle$ and $\psi_b(\mathbf{r}) = \langle r|b\rangle$. For orbitals with s -symmetry, only the $s_{1/2}$ orbital will have substantial size due to the $\delta_T(r)$ function, which limits the important contributions to distances less than or equal to the Thomson radius. We assume that only the s -orbitals contribute to the contact interaction. s -orbitals are spherically symmetric, so that the angular part of the integral becomes

$$\int d\Omega [\boldsymbol{\sigma} \cdot \mathbf{I} - (\boldsymbol{\sigma} \cdot \hat{\mathbf{r}})(\mathbf{I} \cdot \hat{\mathbf{r}})] = \frac{8\pi}{3} \boldsymbol{\sigma} \cdot \mathbf{I}. \quad (2.62)$$

A Hamiltonian for the contact term giving equivalent matrix elements can thus be written in a simplified form as

$$H_c = \frac{8\pi}{3} \frac{\mu_0}{4\pi} \mu_B \gamma \delta_T(r) \boldsymbol{\sigma} \cdot \mathbf{I}, \quad (2.63)$$

which is typically called the Fermi contact interaction. By using $\mathbf{S} = \boldsymbol{\sigma}/2$, the expression can be written as

$$H_c = \frac{4\mu_0}{3} \mu_B \gamma \delta_T(r) \mathbf{S} \cdot \mathbf{I}. \quad (2.64)$$

For an electron in the orbital ground state, ψ_0 , an effective hyperfine Hamiltonian for the subspace of the orbital ground state can be written as

$$\begin{aligned} H_{c,GS} &= \langle \psi_0 | H_c | \psi_0 \rangle \\ &= \frac{4\mu_0}{3} \mu_B \gamma \sum_r \sum_{r'} \langle \psi_0 | r \rangle \langle r | \delta_T(r) \mathbf{S} \cdot \mathbf{I} | r' \rangle \langle r' | \psi_0 \rangle \\ &= \frac{4\mu_0}{3} \mu_B \gamma \delta_T(r) \mathbf{S} \cdot \mathbf{I} |\psi_0(r)|^2. \end{aligned} \quad (2.65)$$

As $|\psi_0(r)|^2$ is the wave function for an electron in the orbital ground state, in a periodic potential, this corresponds to a Bloch function in a one-electron scheme. If one assumes $r_T = 0$, the expression is given by

$$H_{c,GS} = \frac{4\mu_0}{3} \mu_B \gamma \delta_T(r) \mathbf{S} \cdot \mathbf{I} |\psi_0(\mathbf{R})|^2, \quad (2.66)$$

where \mathbf{R} is the position of a nucleus.

We now consider the dipolar hyperfine interaction, which depends on the magnetic field generated by the nuclear magnetic moment

$$\mathbf{B} = \nabla \times \mathbf{A} = \frac{\mu_0}{4\pi r^3} [3\hat{\mathbf{r}}(\boldsymbol{\mu}_I \cdot \hat{\mathbf{r}}) - \boldsymbol{\mu}_I]. \quad (2.67)$$

Inserting the above expression into Equation (2.53) (using $\boldsymbol{\mu}_I = \gamma \mathbf{I}$) gives

$$H_{dip} = \frac{e\hbar c^2}{\epsilon' + 2mc^2 + e\phi} \frac{\mu_0}{4\pi} \gamma \frac{3(\boldsymbol{\sigma} \cdot \hat{\mathbf{r}})(\mathbf{I} \cdot \hat{\mathbf{r}}) - \boldsymbol{\sigma} \cdot \mathbf{I}}{r^3}. \quad (2.68)$$

Assuming a non-relativistic electron, inserting for ϕ (Equation (2.56)), using $\mathbf{S} = \boldsymbol{\sigma}/2$, and some algebra gives

$$H_{dip} = \frac{2\mu_0}{4\pi} \mu_B \gamma \frac{r}{r + r_T/2} \frac{3(\mathbf{S} \cdot \hat{\mathbf{r}})(\mathbf{I} \cdot \hat{\mathbf{r}}) - \mathbf{S} \cdot \mathbf{I}}{r^3}. \quad (2.69)$$

If we neglect the effect of the finite Thomson radius by setting, $r_T = 0$, the expression becomes

$$H_{dip} = \frac{2\mu_0}{4\pi} \mu_B \gamma \frac{3(\mathbf{S} \cdot \hat{\mathbf{r}})(\mathbf{I} \cdot \hat{\mathbf{r}}) - \mathbf{S} \cdot \mathbf{I}}{r^3}. \quad (2.70)$$

The final hyperfine interaction we consider is the nuclear-orbital interaction for a non-relativistic electron. By inserting for the vector potential, and using $\mathbf{L} = \mathbf{r} \times \mathbf{p}$, Equation (2.54) becomes

$$H_L = \frac{2ec^2}{2mc^2 + Ze^2/(4\pi\epsilon_0 r)} \frac{\mu_0}{4\pi} \left(\frac{\gamma \mathbf{I} \times \mathbf{r}}{r^3} \right) \cdot \mathbf{p}. \quad (2.71)$$

Using $\mathbf{A} \cdot (\mathbf{B} \times \mathbf{C}) = \mathbf{B} \cdot (\mathbf{C} \times \mathbf{A}) = (\mathbf{C} \times \mathbf{A}) \cdot \mathbf{B}$, gives

$$H_L = \frac{2ec^2}{2mc^2 + Ze^2/(4\pi\epsilon_0 r)} \frac{\mu_0}{4\pi r^3} \gamma \mathbf{L} \cdot \mathbf{I}. \quad (2.72)$$

Assuming a non-relativistic electron algebra finally gives

$$H_L = \frac{\mu_0}{4\pi} \frac{2\mu_B \gamma}{r^3} \frac{r}{r + r_T/2} \mathbf{L} \cdot \mathbf{I}. \quad (2.73)$$

2.6.2 Derivation of the Hyperfine Interaction Parameters for an Axial Symmetric System

When neglecting the nuclear-orbital interaction, H_L , the Hamiltonian for the HFI can be written as

$$H = \mathbf{I} \cdot \tilde{\mathbf{A}} \cdot \mathbf{S}, \quad (2.74)$$

where $\tilde{\mathbf{A}}$ is the so-called hyperfine interaction tensor. When including the Fermi contact contribution and the dipolar contribution, the HFI tensor can be written as

$$\tilde{\mathbf{A}} = a + \tilde{\mathbf{B}}, \quad (2.75)$$

where $\sum_{ii} B_{ii} = 0$, i.e., it is traceless. The a term is isotropic and corresponds to the Fermi interaction term (Equation (2.66), with $r_T = 0$),

$$a = \frac{4\mu_0}{3} \mu_B \gamma |\psi_0(\mathbf{R})|^2. \quad (2.76)$$

The tensor $\tilde{\mathbf{B}}$ is anisotropic due to the dipolar term (Equation (2.70), with $r_T = 0$) and consists of the terms

$$B_{ij} = \frac{2\mu_0}{4\pi} \gamma \mu_B \int \left(\frac{3}{r^5} x_i x_j - \frac{1}{r^3} \delta_{ij} \right) |\psi_0(\mathbf{r})|^2 d^3 \mathbf{r}, \quad (2.77)$$

where $i, j = 1, 2, 3$ are cartesian coordinates. In a principal axis system x, y, z , Equation (2.74) can be written as[37]

$$H = a(\mathbf{I} \cdot \mathbf{S}) + B_{xx} I_x S_x + B_{yy} I_y S_y + B_{zz} I_z S_z. \quad (2.78)$$

In a system with axial symmetry², by taking z as the symmetry axis, and defining $B_{zz} = 2b$, so that $B_{xx} = B_{yy} = -b$ (due to the tensor being traceless), Equation (2.78) can be written as

$$\begin{aligned} H &= a(I_x S_x I_y S_y I_z S_z) - b I_x S_x - b I_y S_y + 2b I_z S_z \\ &= (a - b)(I_x S_x + I_y S_y) + (a + 2b) I_z S_z \\ &= A_{\perp} (I_x S_x + I_y S_y) + A_{\parallel} I_z S_z. \end{aligned} \quad (2.79)$$

The HFI tensor is thus given by

$$\tilde{\mathbf{A}} = \begin{bmatrix} A_{\perp} & 0 & 0 \\ 0 & A_{\perp} & 0 \\ 0 & 0 & A_{\parallel} \end{bmatrix}, \quad (2.80)$$

and is completely defined by $A_{\perp} = a - b$ and $A_{\parallel} = a + 2b$, with (using $z = r \cos \theta$)

$$b = \frac{1}{2} B_{zz} = \frac{\mu_0}{4\pi} \mu_B \gamma \int \left(\frac{3 \cos^2 \theta - 1}{r^3} \right) |\psi_0(\mathbf{r})|^2 d^3 \mathbf{r}, \quad (2.81)$$

where θ is the angle between the z -axis and the position vector \mathbf{r} .

²The nucleus lies on at (at least) a three-fold symmetry axis of the electron distribution.

2.6.3 Hyperfine Parameters for a Silicon Quantum Dot With an Additional Electron

This section is based on work done by Assali *et al.*[14]. Consider a conventional fcc cubic cell with a single extra electron at a fixed conduction band minimum \mathbf{k}_i . In this case, the system has axial symmetry with respect to the i -axis, and the derivation above may be used to compute the parameters a and b defining the hyperfine tensor. In bulk silicon the spin-density $\rho_s(\mathbf{r}) = \rho_\uparrow(\mathbf{r}) - \rho_\downarrow(\mathbf{r})$, is equal to zero. Keeping an electron at $\mathbf{k} = \mathbf{k}_z$ at the conduction band minima, gives a non-zero spin-density, so that the spin density of an all-electron calculation can be identified as the charge distribution of the extra electron[14]. Thus, the spin-density can be used as the electron ground state, $\rho_s(\mathbf{r}) = |\psi_0(\mathbf{r})|^2$ when computing a and b . A common dimensionless parameter used to express the degree of localization of the electron at the nucleus[38] can be defined as

$$\eta = \rho_s(\mathbf{R})\Omega, \quad (2.82)$$

where $\rho_s(\mathbf{R})$ is the density at the nucleus and Ω is the volume of the supercell for which the density is computed for.

An electron confined in a QD near a [001] interface has the $\pm k_z$ valleys making up the electronic ground state[14]. Due to symmetry, the k_z and $-k_z$ has the same values for the spin-density. Within the envelope function approach, the electron wave function in a QD is expressed by the bulk ground state wave function multiplied by a modulation function

$$\psi_{QD}(\mathbf{r}) = \psi_0(\mathbf{r})F(\mathbf{r}). \quad (2.83)$$

As the spin-density is identified with the Bloch function squared in a one-electron scheme, $|\psi_0(\mathbf{r})|^2$, this gives (by squaring the above equation)

$$|\psi_{QD}(\mathbf{r})|^2 = |\psi_0(\mathbf{r})|^2|F(\mathbf{r})|^2 = \rho_s(\mathbf{r})|F(\mathbf{r})|^2. \quad (2.84)$$

The envelope function squared is normalized over all space, here the QD, while the spin-density of the bulk is normalized over the primitive unit cell. A contribution of the volume of the primitive unit cell (containing two atoms) must thus be included, giving[39]

$$\rho_s^{QD}(\mathbf{r}) = |F(\mathbf{r})|^2\Omega_{PC}\rho_s(\mathbf{r}), \quad (2.85)$$

where $\rho_s^{PC}(\mathbf{r})$ is the spin-density of a primitive unit cell. The expression is normalized over all space. The isotropic HFI parameter a , from Equation (2.76), due to a nuclear spin at \mathbf{R} is

$$a(\mathbf{R}) = \frac{4\mu_0}{3}\mu_B\gamma\rho_s^{QD}(\mathbf{R}) = \frac{4\mu_0}{3}\mu_B\gamma|F(\mathbf{R})|^2\Omega_{PC}\rho_s(\mathbf{R}), \quad (2.86)$$

which by further simplifying, and defining a_2 as the HFI parameter for a primitive unit cell, gives

$$a(\mathbf{R}) = a_2|F(\mathbf{R})|^2\Omega_{PC}. \quad (2.87)$$

To get the total hyperfine interaction of a QD where every nucleus has a spin, $a(\mathbf{R})$ must be summed over the whole quantum dot,

$$a_{\text{total}} = \sum_{I \in QD} a(\mathbf{R}_I) = \sum_{I \in QD} a_2|F(\mathbf{R}_I)|^2\Omega_{PC}, \quad (2.88)$$

where \mathbf{R}_I is the position of the nuclei. Within a primitive cell, there are two nuclei, so that the sum over a primitive cell is

$$a_{PC,I} = a_2|F(\mathbf{R}_{I,1})|^2\Omega_{PC} + a_2|F(\mathbf{R}_{I,2})|^2\Omega_{PC}, \quad (2.89)$$

where R_1 denotes one of the nuclei, and R_2 the other nucleus. By assuming that the envelope function within a primitive cell is constant, we can write,

$$a_{PC} = 2a_2|F(\mathbf{R}_{PC})|^2\Omega_{PC}. \quad (2.90)$$

The modulation function squared and the total spin density are normalized over all of space (which here is the QD). Using this together with having a QD where every nucleus has a spin, and all the nuclear spins are in the same direction, the total HFI parameter becomes

$$a_{\text{total}} = 2a_2. \quad (2.91)$$

The total HFI parameter can be interpreted in a semi-classical way as an effective magnetic field acting on the electron. In the above derivation, all nuclear spins were taken to be non-zero and in the same direction. A random Overhauser field for the case without polarization can be defined as[14]

$$\delta A = \frac{a_{\text{total}}}{\sqrt{N_s}}, \quad (2.92)$$

where N_s is the number of nuclei with non-zero spin. The decoherence time can be found from the random Overhauser field from

$$T_2^* = \frac{\hbar}{\delta A}. \quad (2.93)$$

Computing b for a quantum dot can be done by splitting the term into two contributions and performing numerical estimates of the envelope function. This is outside of the scope of the thesis, but estimations were performed in Ref. [14]. One contribution is taken to be a "near-field contribution," which is dominated by the anisotropy of the spin density close to the nucleus (within the volume of a primitive cell), giving $\Omega_{PC}|F(\mathbf{R})|^2 b_2$. The other contribution, called the "far-field contribution," can be attributed to nuclear spins randomly located inside of the QD. Zhao *et al.*[26] estimated the envelope functions numerically.

2.7 Density Functional Theory

This section presents density functional theory (DFT). The Kohn-Sham equations are derived, possible basis functions commonly used to implement DFT are discussed, along with exchange-correlation functions. The derivations are mainly based on Ref. [40].

2.7.1 Kohn-Sham Equations

In principle, a quantum system can be solved (i.e., obtaining the eigenvalues and eigenstates of the system) by solving the Schrödinger equation which governs the system. The Schrödinger equation for multiple electrons interacting with multiple nuclei is given by

$$H = -\frac{\hbar^2}{2} \sum_i \frac{\nabla_{\mathbf{R}_i}^2}{M_i} - \frac{\hbar^2}{2} \sum_i \frac{\nabla_{\mathbf{r}_i}^2}{m_e} - \frac{1}{4\pi\epsilon_0} \sum_{i,j} \frac{e^2 Z_i}{|\mathbf{R}_i - \mathbf{r}_j|} + \frac{1}{8\pi\epsilon_0} \sum_{i \neq j} \frac{e^2}{|\mathbf{r}_i - \mathbf{r}_j|} + \frac{1}{8\pi\epsilon_0} \sum_{i \neq j} \frac{e^2 Z_i Z_j}{|\mathbf{R}_i - \mathbf{R}_j|}, \quad (2.94)$$

where \mathbf{R}_i is the position of a nucleus with mass M_i and \mathbf{r}_i is the position of an electron with mass m_e . The first two terms describes the kinetic energy, the third the Coulomb interaction between the electrons and the nuclei, the fourth the Coulomb

energy between electrons and electrons, and the final term between nuclei and nuclei. For a large number of particles this becomes infeasible, so approximations are needed.

In the Born-Oppenheimer approximation, the nuclei are approximated to have a fixed position, as they are much slower than electrons. The kinetic term for the nuclei disappears, and the Coulomb interaction between nuclei and nuclei becomes constant. The Hamiltonian in the Born-Oppenheimer approximation is

$$H = -\frac{\hbar^2}{2} \sum_i \frac{\nabla_{\mathbf{r}_i}^2}{m_e} - \frac{1}{4\pi\epsilon_0} \sum_{ij} \frac{e^2 Z_i}{|\mathbf{R}_i - \mathbf{r}_j|} + \frac{1}{8\pi\epsilon_0} \sum_{i \neq j} \frac{e^2}{|\mathbf{r}_i - \mathbf{r}_j|}. \quad (2.95)$$

Although this is a simplification, it is still too difficult to solve. The method explained here is the density functional theory. DFT is based on the two Hohenberg-Kohn theorems[41] and is commonly used to find properties of interacting many-body systems without using the method of solving the Schrödinger equation. The first Hohenberg-Kohn theorem states that for any system of interacting particles in an external potential, $V_{\text{ext}}(\mathbf{r})$, the potential is determined uniquely (except for a constant) by the ground state particle density $n_0(\mathbf{r})$. The second theorem states that a universal functional for the energy of a system, $E[n]$, in terms of the density, $n(\mathbf{R})$, can be defined and is valid for any external potential. For a particular external potential, the ground state energy of the system is the global minimum value of $E[n]$, and the density that minimizes the functional is the exact ground state density n_0 . Therefore, finding the electron density corresponding to the ground-state wave function will allow obtaining the exact properties of the system. However, no model of the energy functional is provided by the theorem; it only guarantees that it exists.

The second theorem makes it possible to use the variational principle of Rayleigh-Ritz to find the ground-state energy. This principle is used by Kohn and Sham, which gives a practical method for obtaining the ground state density. In this formalism, the interacting system is mapped into a non-interacting system of electrons having the same electron density as the original system. The energy functional of such a system is given by

$$E[n(\mathbf{r})] = T_S[n(\mathbf{r})] + \int V_{\text{eff}}(\mathbf{r})n(\mathbf{r})d^3r, \quad (2.96)$$

where

$$T_S[n(\mathbf{r})] = \sum_i \left\langle \phi_i \left| -\frac{\nabla^2}{2} \right| \phi_i \right\rangle \quad (2.97)$$

is the kinetic energy of a system of non-interacting electrons with density $n(\mathbf{r}) = \rho(\mathbf{r}) = \sum_i^N \phi_i^*(\mathbf{r})\phi_i(\mathbf{r})$ with the sum being over the N electrons in the crystal. The effective potential is given by

$$V_{\text{eff}}(\mathbf{r}) = V_{\text{ext}}(\mathbf{r}) + V_H(\mathbf{r}) + V_{XC}(\mathbf{r}), \quad (2.98)$$

where $V_{\text{ext}}(\mathbf{r})$ is the Coulomb interaction between an electron and the atomic nuclei, $V_H(\mathbf{r})$ is the Coulomb interaction between the electrons (Hartree term) and

$$V_{XC}(\mathbf{r}) = \frac{\delta E_{XC}[n(\mathbf{r})]}{\delta n(\mathbf{r})} \quad (2.99)$$

is the exchange-correlation potential (XC potential), defined as the functional derivative of the XC functional E_{XC} . The XC potential describes all quantum mechanical effects. ϕ is called the Kohn-Sham (KS) orbitals/functions and is given from the Kohn-Sham equations[42]

$$V^{\text{KS}}\phi_i(\mathbf{r}) = \left[-\frac{\hbar^2}{2m_e}\nabla^2 + V_{\text{eff}}(\mathbf{r}) \right] \phi_i(\mathbf{r}) = \varepsilon_i\phi_i(\mathbf{r}), \quad (2.100)$$

where ε are the Kohn-Sham eigenvalues. If a magnetic field is applied to the system, the density will be modified, so that $\rho(\mathbf{r}) = \rho_{\uparrow}(\mathbf{r}) + \rho_{\downarrow}(\mathbf{r})$. All terms remain the same except for a different exchange-correlation potential which now has a dependence on both spins[43], and there are now Kohn-Sham equations for each spin state σ giving two sets of KS-equations.

2.7.2 Solving the Kohn-Sham Equations

With an explicit expression for approximating the KS-equations, they can now be solved. However, the potential needs to be defined to solve them, and the potential depends on the density (i.e., the KS-orbitals squared). So we need the orbitals to find the potential and the potential to find the orbitals. An approach to resolve this issue is to use a self-consistent field (SCF) cycle. First, an initial density is used to compute an initial potential, giving the orbitals and thus a density. It is very likely that this density will not equate to the initial density, so the density must be modified in some way until the density used to compute the potential is (in practice approximately) equal to the density found by solving the KS-equation. This means that the solution must be self-consistent. Having obtained the density, it is

considered to be the ground-state electron density and can be used to compute the total energy of the system. It should be noted that the KS-orbitals that are found do not have any physical meaning, but mathematically they are single-particle orbitals. In a periodic system, like a crystal, we recall from Section 2.4 that Bloch functions are the physical solutions to the systems. However, in general one cannot simply assume that the computed KS-orbitals, $\phi_{\mathbf{k}}(\mathbf{r})$, are equal to the Bloch functions, $\psi_{\mathbf{k}}(\mathbf{r})$. Only the density obtained from DFT has any physical meaning.

In practice, what is done to find the KS-orbitals as described above is to find the coefficients c_{α}^{μ} in a given basis set with functions ϕ_{α} , such that

$$\phi_{\mu}(\mathbf{r}) = \sum_{\alpha} c_{\alpha}^{\mu} \phi_{\alpha}, \quad (2.101)$$

where $\mu = \{n, \sigma, \mathbf{k}\}$, with n being the band index, σ the spin, and \mathbf{k} the wave vector. Inserting Equation (2.101) into Equation (2.100) and moving to the left hand side gives

$$\sum_{\alpha} [V^{KS} |\phi_{\alpha}(\mathbf{r})\rangle - \epsilon_n |\phi_{\alpha}(\mathbf{r})\rangle] c_{\alpha}^{\mu} = 0. \quad (2.102)$$

Left multiplying by $\langle \phi_{\beta}(\mathbf{r}) |$ gives

$$\sum_{\alpha} [\langle \phi_{\beta}(\mathbf{r}) | V^{KS} | \phi_{\alpha}(\mathbf{r}) \rangle - \epsilon_n \langle \phi_{\beta}(\mathbf{r}) | \phi_{\alpha}(\mathbf{r}) \rangle] c_{\alpha}^{\mu} = 0. \quad (2.103)$$

Defining $\langle \phi_{\alpha} | \phi_{\beta} \rangle = S_{\alpha\beta}$ and $V_{\alpha\beta}^{KS} = \langle \phi_{\beta}(\mathbf{r}) | V^{KS} | \phi_{\alpha}(\mathbf{r}) \rangle$ gives a secular equation, $[V^{KS} - \epsilon_n \mathbf{S}] \mathbf{c}^{\mu} = 0$. The equation is solved at each k-point.

2.7.3 Basis Functions in DFT

The Augmented plane wave method

The basis functions used to compute the coefficients will impact the accuracy and computational efficiency of a program. One such basis set is the augmented plane wave (APW) method, first proposed by Slater[44]. The method uses different plane waves depending on the region of space. Around each atom, a sphere of radius R_{MT} (called a muffin-tin sphere) is drawn. Within the sphere (i.e., very close to the nucleus) the electrons behave similarly to as if they were bound to a free atom. Outside of this region (called the interstitial region, I) they are approximately like

free electrons, and plane waves are used to describe the electrons. The basis set is defined as

$$\phi_{\mu\mathbf{K}}(\mathbf{r}) = \begin{cases} \frac{1}{\sqrt{V}} e^{i(\mathbf{k}+\mathbf{K})\cdot\mathbf{r}} & \mathbf{r} \in I \\ \sum_L A_{\mu L\mathbf{K}}^\alpha u_\ell^\alpha(r', E) Y_L(\hat{r}') & \mathbf{r} \in S_\alpha, \end{cases} \quad (2.104)$$

where \mathbf{K} is a reciprocal lattice vector, \mathbf{r}' is the position relative to the center of each sphere, and r' is the length of \mathbf{r}' . The angles θ' and ϕ' specifying the direction of \mathbf{r}' is given as \hat{r}' . $A_{\mu L\mathbf{K}}^\alpha$ are coefficients determined by the condition that the interstitial and spherical parts has to be equal at the sphere boundary, u_ℓ^α are the solutions to the radial part of the Schrödinger equation for a free atom α . $Y_L(\hat{r})$ are the spherical harmonics. The total wave function is expanded in the basis set as

$$\phi_\mu(\mathbf{r}) = \sum_{\mathbf{K}} C_\mu(\mathbf{K}) \phi_{\mu\mathbf{K}}(\mathbf{r}). \quad (2.105)$$

The APW method is not used in practice anymore, as the radial functions are energy-dependent. For the basis functions to be efficient, the radial functions must be picked within a small energy window. A new basis function set must thus be constructed for each energy window, making it a time-consuming method.

The energy dependence can be handled by a local orbital (lo), as introduced by Sjöstedt *et al.*[45], called the APW+lo method. The method is based on the original APW method, but adding local orbitals for $l \leq 3$. The local orbitals are given by

$$\phi_{Ln\sigma}^{\text{lo}}(\mathbf{r}) = \begin{cases} 0 & \mathbf{r} \notin S_\alpha \\ \left[A_{Ln\sigma}^{\text{lo},\alpha} u_\ell^\alpha(r', E_{1,\ell}^\alpha) + B_{Ln\sigma}^{\text{lo},\alpha} \dot{u}_\ell^\alpha(r', E_{1,\ell}^\alpha) \right] Y_m^\ell(\hat{r}') & \mathbf{r} \in S_\alpha. \end{cases} \quad (2.106)$$

The coefficients A and B are determined by normalization and from requiring that the local orbital is equal to zero at the sphere boundary. Note that they are not dependent on k . For the APW+lo method, the majority of the basis functions only have terms proportional to u_l , not its derivative.

The linearized augmented plane wave method

To improve on the method, the linearization energy, E_0 is introduced. If u_l^α has been calculated at some energy E_0 , a Taylor expansion can be used to compute energies close to it

$$u_l^\alpha(r', \epsilon) = u_l^\alpha(r', E_0) + (E_0 - \epsilon) \frac{\partial u_l^\alpha(r', E)}{\partial E} \Big|_{E=E_0} + \dots, \quad (2.107)$$

which can be written as

$$E_l^\alpha \approx u_l^\alpha(r', E_0) + (E_0 - \epsilon)\dot{u}_l^\alpha(r', E_0). \quad (2.108)$$

Inserting into Equation (2.104) and defining a new parameter $B_{\mu L \mathbf{K}}^\alpha$ to encompass the unknown term $(E_0 - \epsilon)$, gives the basis set

$$\phi_{\mu \mathbf{K}}(\mathbf{r}) = \begin{cases} \frac{1}{\sqrt{V}} e^{i(\mathbf{k} + \mathbf{K}) \cdot \mathbf{r}} & \mathbf{r} \in I \\ \sum_L [A_{\mu L \mathbf{K}}^\alpha u_\ell^\alpha(r', E_0) + B_{\mu L \mathbf{K}}^\alpha \dot{u}_\ell^\alpha(r', E_0)] Y_L(\hat{r}') & \mathbf{r} \in S_\alpha. \end{cases} \quad (2.109)$$

$A_{\mu L \mathbf{K}}^\alpha$ and $B_{\mu L \mathbf{K}}^\alpha$ are determined by the condition that at the sphere boundary, the function and the slope from the interstitial and within the sphere has to be equal. Further to define the Linearized Augmented Plane Wave method (LAPW)[46], a set of well-chosen linearization energies should be chosen for small l , instead of one universal value, giving

$$\phi_{\mu \mathbf{K}}(\mathbf{r}) = \begin{cases} \frac{1}{\sqrt{V}} e^{i(\mathbf{k} + \mathbf{K}) \cdot \mathbf{r}} & \mathbf{r} \in I \\ \sum_L [A_{\mu L \mathbf{K}}^\alpha u_\ell^\alpha(r', E_l^\alpha) + B_{\mu L \mathbf{K}}^\alpha \dot{u}_\ell^\alpha(r', E_l^\alpha)] Y_L(\hat{r}') & \mathbf{r} \in S_\alpha. \end{cases} \quad (2.110)$$

The wave function is given by

$$\phi_\mu(\mathbf{r}) = \sum_{\mathbf{K}} C_\mu(\mathbf{K}) \phi_{\mu \mathbf{K}}(\mathbf{r}), \quad (2.111)$$

as for the APW case.

A disadvantage for the LAPW method is that for localized states where \dot{u}_l/u_l at R_{MT} are very large, it will require a very large number of plane waves to satisfy the constraint of being continuously differentiable at the sphere boundary.

Also for the LAPW method, local orbitals (denoted LOs, not lo), are added. These orbitals solved the issue with semi-core states, i.e., low-lying valence states. Choosing the linearization energies for these states is not clear. Thus, another type of orbital is added, where the radial functions are calculated at the semi-core energy $E_l^{LO, \alpha}$. A local orbital is a linear combination of two radial functions at two linearization energies and one energy derivative. The definition is

$$\phi_L^{LO}(\mathbf{r}) = \left[A_{\ell m}^{\alpha, LO} u_\ell^\alpha(r', E_{1, \ell}^\alpha) + B_{\ell m}^{\alpha, LO} \dot{u}_\ell^\alpha(r', E_{1, \ell}^\alpha) + C_{\ell m}^{\alpha, LO} u_\ell^\alpha(r', E_{2, \ell}^\alpha) \right] Y_m^\ell(\hat{r}') \quad (2.112)$$

inside the sphere, and zero outside of the sphere. The coefficients are determined by the requirement of the orbitals being normalized and zero value and slope at the sphere boundary.

The true radial function varies most for more localized states at larger distances from the nucleus. This can lead to a significant dependence of the results on R_{MT} . This issue can be resolved by adding another type of LO, involving the second energy derivative of u_ℓ^α , called an HDLO[47], defined as

$$\phi_L^{\alpha, \text{HDLO}}(\mathbf{r}) = \begin{cases} \left[A_L^{\alpha, \text{HDLO}} u_\ell^\alpha(r', E_\ell^\alpha) + C_L^{\alpha, \text{HDLO}} \ddot{u}_\ell^\alpha(r', E_\ell^\alpha) \right] Y_L(\hat{r}'), & \mathbf{r} \in S_t \\ 0, & \mathbf{r} \in I. \end{cases} \quad (2.113)$$

2.7.4 Exchange-Correlation Functionals

The main challenge from here is that the XC potential is unknown and must be approximated. The accuracy of the DFT computation, therefore, depends on the XC potential used, and several different potentials for different systems have been developed. There are several types of XC-potentials, but the most simple type is the local density approximation (LDA). The potential is defined as

$$V_{XC}^{\text{LDA}}(\mathbf{r}) = V_{XC}^{\text{el. gas}}[n(\mathbf{r})], \quad (2.114)$$

so that the the XC-potential at a position \mathbf{r} is that of a homogeneous electron gas with the electron density at that point in space.

Another well-known class of approximations is the generalized gradient approximation (GGA), where both the local density and the local gradient of the electron density are included. A common XC-potential used is the Perdew, Burke and Ernzerhof (PBE) potential[48].

An issue with DFT is that it underestimates the band gaps of semiconductors and insulators. An exchange-correlation potential proposed by Becke and Johnson[49], and later modified by Tran and Blaha[50], called the modified Becke Johnson (mBJ) potential agrees well with experimental values. The XC-potential depends on two parameters α and β , and a parametrization suggested by Koller, Tran, and Blaha (referred to as Koller parametrization from hereon) has been shown to be accurate for semiconductors with band gaps up to 7 eV[51]. For silicon the original parametrization by Tran and Blaha gave a value closer to experimentally obtained values.

Chapter 3

Method

In this section the program WIEN2k[16] (version 19.1) is discussed. The method used to perform a standard spin-polarized computation using SOC for silicon is explained. Further, the method used to compute the isotropic hyperfine interaction, a , in silicon supercells of various sizes is explained in detail.

3.1 WIEN2k

WIEN2k[16] is a commercial DFT program using the linearized augmented plane wave method, which allows for full-potential calculations. In this section, the DFT version implemented in WIEN2k will be discussed. The WIEN2k version discussed is the 19.2 version, released in 2019. More details on the implementation can be found in the User Guide (UG), which can be found online[52] (note that this UG is of the newest version, 21.4). The UG is also the main reference for this section.

3.1.1 DFT Implementation

DFT is implemented by solving the KS equations as explained in the previous sections. The convergence of the basis set is controlled by a cutoff parameter $R_{mt}K_{max}$. Valence states are treated using the scalar relativistic approximation of the second variational method. WIEN2k implements and recommends using a combination of the APW+lo and LAPW, including local orbitals (LOs) for semi-core states, and HDLOs, and can thus be summarized as a (L)APW+lo+LO+HDLO method. In general the LAPW method is used, but this requires a higher K_{max}

than APW+lo+LO for some states. For those states, which is valence f- and d-states, and states in atoms that have a muffin tin sphere that is much smaller than other spheres in the unit cell, APW+lo+LO is used. The LOs for APW+lo method has a different definition than for LAPW, where no derivative is included,

$$\phi_{\alpha,LO}^{\ell m}(\vec{r}) = \begin{cases} 0 & \vec{r} \notin S_{\alpha} \\ \left(A_{\ell m}^{\alpha,LO} u_{\ell}^{\alpha}(r', E_{1,\ell}^{\alpha}) + C_{\ell m}^{\alpha,LO} u_{\ell}^{\alpha}(r', E_{2,\ell}^{\alpha}) \right) Y_m^{\ell}(\hat{r}') & \vec{r} \in S_{\alpha} \end{cases} \quad (3.1)$$

Relativistic effects are important for the core states and are included by numerically solving the Dirac equation for a spherically symmetric potential. Semi-core and valence electrons are treated scalar relativistically but neglecting spin-orbit interactions. These can, however, be included in a second variational step using the scalar-relativistic orbitals as a basis.

3.1.2 Initializing a Calculation

Before performing a computation, it must be initialized. All computations should be initialized and ran from separate folders (which can be stored anywhere on the system) referred to as `case`, where `case` is replaced by an appropriate name (e.g., Si for silicon) in an actual computation. All computations are done by separate programs. A program can be run by the `x` script, by writing `x program`. Each program reads and/or writes to `case.inX` and `case.outputX` files (where X labels the program). The programs for the SCF cycle also writes a `case.scfX` file containing the most important output.

To start a standard computation, all that must be given to the program is the structure of the crystal. This will be given as a file called `case.struct`, which is a formatted file containing the information needed for the program. From the terminal, this file may be created using the command `makestruct_lapw` which must be called within the same folder as where the `case.struct` file is to be placed (i.e., within the case folder). After supplying the `struct` file, the DFT computation must be initialized. The initialization will be done by running six different programs, `SETRMT`, `NN`, `SGROUP`, `SYMMETRY`, `LSTART`, `KGEN`, and `DSTART`. The script `init_lapw` will run all these programs with interactive input. `init_lapw -b` will run with default inputs. All programs are described in detail in the User Guide but are summarized below.

NN

The program uses the required `case.struct` file to calculate the nearest-neighbor distances of all atoms in the unit cell. It also checks that the corresponding atomic spheres are not overlapping and that equivalent atoms are specified correctly. The program will output a new structure file, `case.struct_nn` if the equivalent atoms specified in `case.struct` do not have equivalent environments. Therefore, the program can help with, e.g., creating supercells.

SGROUP

The spacegroup of the unit cell is determined from the `struct`-file. It can also produce a new `struct` file, `case.struct_sgroup`, which is, again, helpful for supercells.

SYMMETRY

Symmetry uses the information about lattice type, atomic positions from the structure file to generate the symmetry operations of the space group. The LM expansion for the lattice harmonics is determined, in addition to the local rotation matrix.

LSTART

Generates atomic densities, $H\psi_{nl} = E_{nl}\psi_{nl}$ and input files needed for the SCF cycle. It also creates the atomic potentials and asks the user to interactively specify the XC-functional. Some of the possible options are LDA, PBE, WC, and PBESOL. An energy cut-off is also asked for, which is the energy-value (in Rydberg) used to separate the core and valence states. The default (and usually a good choice) is -6.0 Ry.

KGEN

The program is used to generate a list of k-values in the irreducible Brillouin zone (IBZ). The IBZ consists of all points which are symmetric for the given structure. It interactively asks for the total number of k-point in the total BZ (not the IBZ).

DSTART

The program generates the starting charge density, ρ , from a superposition of the atomic densities generated in LSTART.

3.1.3 Running an SCF cycle

When the initialization is performed with no errors present, the initial density ρ_{in} has been generated and is given as an input for the SCF cycle. The entire cycle can be performed using the script `run_lapw`. The main programs that are run (in order) are LAPW0, LAPW1, LAPW2, LCORE, and MIXER, but depending on flags given to `run_lapw` additional programs will be run. The cycle will continue until convergence is reached.

LAPW0

The program takes a density ρ_{new} as input and computes the total potential V_{tot} , which is the sum of the Coulomb potential, V_c and the XC-potential V_{xc} . The methods used for the computations are explained in the UG.

LAPW1

With the potential computed, the Hamiltonian and overlap matrix is set up for the valence states, and the eigenvalues and eigenvectors are found by diagonalization. Both the LAPW basis set and the APW+lo (if needed) can be used and mixed as explained in previous sections. LOs can be specified, in addition to HDLOs, in the input file, `case.in1`.

LAPW2

The program calculates the Fermi-energy and the expansion of the electronic charge densities for each occupied state and each k-vector, $\rho_{valence} = \sum_{E_k < E_F} \psi_k^* \psi_k$. The input file `case.in2` can be used to specify the cut-off for defining the range of occupied states (by the `-all X Y flag`) and specifying the number of electrons per unit cell in the specified energy range.

LCORE

Computes the core states for the current spherical part of the potential, $H\psi_{nl} = E_{nl}\psi_{nl}$, giving ρ_{core} and E_{core} .

MIXER

The electron densities of the core, semi-core and valence states are added, giving the output density $\rho_{in} = \rho_{valence} + \rho_{core}$. Normalization of the density is checked and corrected by adding a constant charge density in the interstitial. Using the new density leads to instabilities in the SCF cycle, and stabilization is done by mixing the output density with the input density. This is then used to create a new density which is used in the next iteration of the cycle. An example of a simple mixing scheme, which is one of several implemented in WIEN2k, by Pratt is

$$\rho_{new}(r) = (1 - Q)\rho_{in}(r) + Q\rho_{out}(r), \quad (3.2)$$

where Q is a mixing factor. The mixing scheme used can be specified in the input file, `case.inm`, where the possible schemes are explained in the UG. It is also possible to specify a background charge to the cell.

3.1.4 Spin-Polarized Calculations

A spin-polarized computation can be run by specifying the `-up` and `-dn` flag on the needed programs. For initialization, this can be done by setting `init_lapw -sp`, and for running a cycle, this is done by running `runsp_lapw`. If running the programs individually, they usually have to be run for both the `-up` and the `-dn` flag separately.

3.1.5 Spin-Orbit Coupling

Spin-orbit coupling (SOC) is not included by default. The program `LAPWSO` includes SOC in a second variational procedure. The procedure uses the scalar-relativistic wave functions from `LAPW1`. An additional basis function with a $p_{1/2}$ radial wave function is also provided. Further details on the implementation can be found from the WIEN2k web page (also included in the program download) written by Novák[53].

Running `init_so_lapw` helps create or modify input files, `case.inso`, `case.in1`, `case.in2c`. In a spin-polarized computation, the coupling can reduce symmetry, or it could be that equivalent atoms are no longer equivalent. It is then necessary to consider a larger part of the BZ, i.e., increasing the number of points in `case.klist`. LAPW2 should also be modified, as the potential has lower symmetry. The program `symmetso`, which can be called from the initialization program, can help to find the proper symmetries and setup the input files. The files `case.struct`, `.klist`, `.kgen`, `.in2c` (SOC eigenvectors are complex) and `.in1` can change. It is only necessary to run `x lapwso` with the `-up` flag for a spin-polarized computation as SOC will mix the spin up and spin down states in a single calculation.

The input file `case.inso` will be generated by `init_so_lapw`, but can also be specified manually. The most important parameters in this file is the vector describing the direction of magnetization (line 4), the number of atoms, `nlr`, and which atoms should have extra $p_{1/2}$ basis functions (line 5 and 6-`nlr`).

3.1.6 Creating Supercells

Supercells are cells that are larger than a unit cell and can be constructed by translating the unit cell in space until the wanted size is obtained. There are several ways to create supercells in WIEN2k. The first and most straightforward method is to use the `SUPERCELL` program. The program takes a structure file as input and asks interactively which type of supercell is wanted (F, B, P). Then the multiplicity in the x , y , and z directions must be written to the program. Vacuum can also be added to model lower-dimensional structures. The program `VESTA`[54] can also be used to create supercells. To create supercells in `VESTA` a regular unit cell must be constructed, and then the transformation matrix is changed from an identity matrix to only having off-diagonal scaling factors. The files are created in the `.cif` format which WIEN2k can convert to a `struct` file using `cif2struct`.

After the supercell has been created, it must be modified before running the initialization. If not, then `SGROUP` will reduce the supercell back to the original structure. Some broken symmetry must be introduced. If the same lattice structure is wanted, one or more atoms must be given a different label so that an independent atom is created. If all multiplicities are larger than 1, at least one atom must be

moved to a separate line. `NONEQUIV`. `ATOMS` on line 2 must also be changed to reflect the new number of non-equivalent atoms.

The calculation must now be initialized, as follows:

1. Run `NN`. If warnings are printed to the terminal, accept the new `case.struct_nn` file by copying it to `case.struct`. Repeat until no warnings.
2. Run `SGROUP`. Open `case.outputsgroup`. If any warnings, use `case.struct_sgroup`. Repeat until no errors.
3. Run `SYMMETRY`. Check `case.outputs`. If warnings, use `case.struct_st`. Repeat until no errors.
4. Initialize in with `init_lapw` (and any additional flags needed for the particular computation).

It is useful to then open the `case.struct` file and compare it with the original struct file to ensure that the positions are the same.

3.1.7 Calculating Band Structure Using Spaghetti

The program `spaghetti` can be used after performing an SCF cycle to obtain the band structure of a system. The input files needed are `case.insp` and `case.klist_band`, and must be defined by the user. `case.insp` defines the properties of the plot (most importantly the energy range and the Fermi level), and `case.klist_band` defines a new k-mesh for the points for which the energy is to be computed. There are template files available in the `SRC_templates` folder, but examples from computations in this thesis can be found in Appendix A. The commands used to complete a (non-spin-polarized) calculation is `x lapw1 -band` and `x spaghetti`. The plot can then be found in `case.spaghetti_ps`, and the bandgap can be found under the label `:GAP` in `case.scf`.

3.1.8 Charged Supercells

To create a charged supercell, in principle adding or removing one electron, the regular (neutral) supercell must first be initialized, and an SCF cycle is done until

convergence is reached. After, in the field for the number of electrons, `NE`, on the second line of `case.in2(c)` must be edited. If one electron is to be added, this number is incremented by one, and if one electron is to be removed, it is decremented by one. Then the first line in `case.inm` is edited so that the (default) value of `MSR1` is changed to `BROYD`, and the second line, setting the background charge is either `1.0` (if an electron was added) or `-1.0` (if an electron was removed). Now another SCF cycle must be performed, which gives the charged system.

3.1.9 Using the Modified Becke-Johnson XC-Potential

In order to resolve the issue of underestimating the bandgap, the mBJ potential can be used. A procedure for a computation with spin-polarization and SOC using the mBJ XC potential is shown Appendix A.5 which also provides further details on the steps performed in one cycle. First, a regular spin-polarized and SOC computation is performed, and the mBJ potential is then added. The first run of `init_mbj_lapw` is done to prepare and change the necessary files. Then, one SCF cycle is run to generate the required files. Then another run of `init_mbj_lapw` is done, where the program asks for input. The option `0` is chosen, which are the original mBJ values from Tran and Blaha. Finally, a SCF computation is performed. Note that it will usually require a lot of cycles to achieve a converged computation.

To add charge when using the mBJ potential the steps above must first be performed. In addition to changing `case.in2(c)` and `case.inm` the file `case.inm_vresp` must be edited in the same way as `case.inm`.

3.1.10 Computing the Contact Hyperfine Interaction

WIEN2k implements a method for computing the hyperfine interactions, as described by Novák in Ref. [55]. To compute the contact interaction, the program `MIXER` is used, which calls the function `hyperf`. The function computes the average electron density from the first point in the spherical mesh to the Thomson radius,

$$\text{hyperf} = \frac{q_{el}}{\frac{4}{3}\pi(r_T^3 - r_1^3)}, \quad (3.3)$$

where

$$q_{el} = \int_{r_1}^{r_T} \rho_{00}(r) dr, \quad (3.4)$$

where r_T is the Thomson radius, r_1 is the first point in the spherical mesh of the atom. This is done for valence, semi-core, core electrons, and total density. The total density can be used to compute the hyperfine parameter a , as defined in Equation (2.76). The density at the nucleus only is also computed by MIXER.

3.1.11 Producing Density Plots Using LAPW5

LAPW5 generates the charge density in a specific plane of the crystal by taking an input file `case.in5` which specifies the plane and properties of the densities which are generated. The program outputs the electron density in the file `case.rho`. It is possible to produce both up, down, and total densities, in addition to spin densities. An example of an input file used to generate spin densities in a (100) plane of an 8-atom silicon supercell is shown in Appendix B.4.

3.1.12 Numerical Considerations

The KS-equations and DFT are limited by the need for solving equations that are discrete. It is important that the computations performed are well-converged. There are several parameters that could impact the convergence and should be discussed.

Integrals on the form

$$\bar{g} = \frac{V_{\text{cell}}}{8\pi^3} \int_{\text{BZ}} g(\mathbf{k}) d\mathbf{k}, \quad (3.5)$$

defined in k -space has to be evaluated for the k -points defined in the BZ. As it is a numerical method, the number of k -points is finite, and choosing a dense enough k -mesh is important for achieving accurate results. The process of determining the k -mesh is often called BZ sampling. It should be noted that it is not necessarily the number of k -points that is important, but their spacing in k -space. A commonly used method for BZ sampling is the Monkhorst-Pack method[56], where the coordinates of the points are given by

$$\mathbf{k}_j = x_{1j}\mathbf{b}_1 + x_{2j}\mathbf{b}_2 + x_{3j}\mathbf{b}_3, \quad (3.6)$$

where \mathbf{b}_j are reciprocal lattice vectors, and

$$x_{ij} = \frac{l_i}{n_j}, i = 1, \dots, n_j, \quad (3.7)$$

where l_i are the lengths of the reciprocal lattice vectors \mathbf{b}_i . n_j determines the number of points in the mesh. Using these points will give a homogeneous mesh which is spread out over the whole BZ. A large real space cell corresponds to a small k -space cell, as their volumes are inversely related. Therefore, for a small cell, a larger number of k -points is needed than for a large cell.

The (L)APW method used basis sets which in theory are infinite expansions. However, in practice, one has to use a finite set of basis functions. A parameter used in WIEN2k to determine the size of the basis set is $R_{mt}K_{max}$, where R_{mt} is the size of the smallest atomic sphere, and K_{max} is the largest k -value included in the plane-wave expansion. If the value is too small, the computation will not properly converge, but if it is too large, it will be unnecessarily time-consuming.

A convergence test should be performed for these parameters to determine the necessary values for the computation at hand. This is often done with respect to the total energy, but if other values are estimated, they should also be checked against the parameters. It should also be noted that achieving a well-converged DFT computation only means that the result is correct up to the approximations used to derive the KS-equations.

3.2 Bulk Silicon Computations

A self-consistent calculation including spin-polarization and spin-orbit coupling for a silicon structure using lattice parameters of $a = b = c = 5.43 \text{ \AA}$ was performed with the structure file generated using `makestruct.lapw`, which can be found in Appendix A.1. The entire procedure is shown in Appendix A.2. Convergence of k -mesh size (see Appendix A.3) and $R_{mt}K_{max}$ (see Appendix A.4) was checked with respect to total energy to ensure a properly converged calculation to within 0.0001 Ry, using the PBE functional. Unless otherwise stated, the parameters used are those of the default values of WIEN2k. The Fermi energy was found from the `case.scf` file, from the `:FER` label. Further, the band structure was computed using the `SPAGHETTI` program and k -values in `case.klist_band` (which is included in Appendix B.2 and B.3). The bandgap was found from the `:GAP` label in `case.scf`. To obtain the lowest energy of the first unoccupied band, the label `:BAN` in `case.scf` was found

for the lowest band, which is unoccupied. In addition to the PBE functional, the bandgap was computed for the LDA and mBJ (see Appendix A.5) functionals.

3.3 Isotropic Hyperfine Interaction

The method explained here is based on Ref. [14], but here details on how the computation was performed are presented. The procedure is summarized in Figure 3.1, and all steps performed are shown in Appendix A.6.

First, a supercell of the wanted size was created. The number of atoms in the five supercells considered was $N = 8, 16, 32, 54, 64$. The supercells used were created using VESTA[54], and are shown in Appendix D. They were initialized using the method explained in Section 3.1.6. The first step after initialization was to perform a SCF cycle for the supercell, including spin polarization and SOC. After the cycle, an electron was added to the supercell. To create a negatively charged supercell containing one extra electron, the files `case.in2` and `case.inm` were modified. In `case.in2`, the number of electrons was increased by 1. In `case.inm`, the mixing parameter was changed to `BROYD`, and 1.00 was added to create a positive background charge so that the entire unit cell was neutral. Another SCF cycle was then performed for the charged supercell. Before further proceeding with the computations, the conduction band minima was found. The 8-atom supercell without charge was used with 300 k -points from $\mathbf{k} = (0, 0, 0.1400)$ to $\mathbf{k} = (0, 0, 0.1699)$ (increasing k_z by 0.001 for each point) to determine the k_z -value of the conduction band minima. This was done by finding the lowest eigenvalue of the lowest conduction band from `case.output2up` (under the line saying "Bandranges (emin-emax) and occupancy"), which is the first band that is unoccupied. The eigenvalue found was searched for in `case.output1up` which gives the k -point that has this eigenvalue.

Further, the electron must be constrained to be placed in the lowest-lying conduction band. The total potential was computed from `LAPW0`. After computing the total potential, the Hamiltonian was written for a fixed k -point by removing all points from `case.klist` except the one found for the minima. As the k -points are written for the IBZ, meaning that a point in the $\Gamma - X$ direction corresponds to six points in the full BZ, the weight of the k -point for the minima was changed from

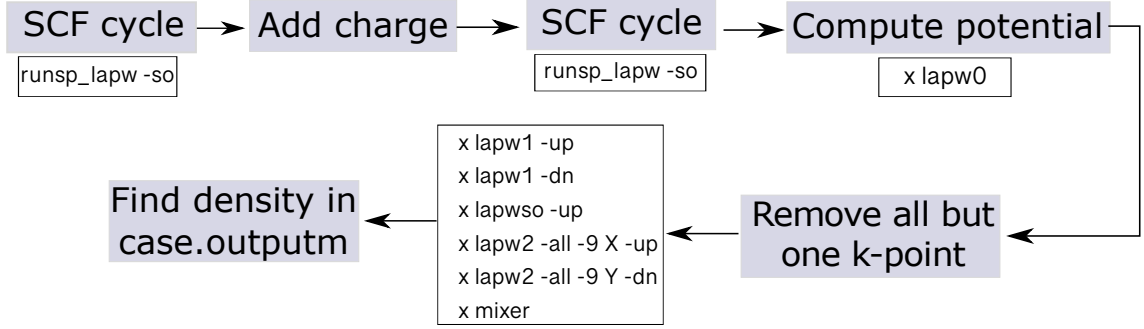


Figure 3.1: Visual summary of the procedure used for computing the HFI parameters for silicon supercells with one additional electron placed in the conduction band minima. A SCF cycle including SOC was performed, and charge was added. Then another SCF cycle was completed. Further, the potential of the converged charge density was computed using LAPW0. Then all k -points but the one for the conduction band minima was removed from `case.klist`, and the eigenvalues and states were computed using LAPW1 and LAPWSO. Then LAPW2 was ran, restricting the energy of the bands occupied using the `all` flag (or editing `case.in2(c)`). Finally MIXER was ran and the spin-densities obtained from `case.outputm`.

6.0 to 1.0. To obtain the point in the $+z$ direction, the point chosen was the one with 0 in the x and y directions. Then the eigenvalues and eigenvectors were computed using LAPW1. LAPW2 was then run for energies between two values by using the flag `-all X Y`¹. To include all the valence bands, `X` was set to -9. For the spin-up case, `Y` was set to a value slightly higher than the eigenvalue of the conduction band minima (to ensure that it is included). The precision using the flag is limited to four decimals. If the energy difference between the lowest-lying conduction band and the next one is smaller than that, the file `case.in2(c)` must be modified², and `x lapw2` ran without the `-all` flag. For the spin-down case, `Y` was set to a value slightly higher than the eigenvalue of the valence band. To ensure the correct bands were included, the files `case.output2dn/up` were checked. Finally, mixer was run

¹As the k -point of the conduction band minima typically is not included in the original k -mesh, LAPW2 usually has to be run twice, first with an estimate of what `X` and `Y` to obtain the exact values which will place the electron in the conduction band from the `case.output2dn/up` files.

²The `case.in2(c)` must be modified by changing from `TETRA 0.000` to `ALL X` on the third line, where `X` is slightly higher than the lowest-lying conduction band but not large enough so that the next band is included.

to compute the densities at the nucleus and around the Thomson radius, with the results found in `case.outputm`.

The density around the Thomson radius was found under the line "SPINDENSITIES AT THE NUCLEUS (THOMSON) FOR ATOM x". The first value under TOTAL was subtracted from the second, giving ρ_s in units of $1/a_0^3$, where $a_0 = 5.2917725 \cdot 10^{-11}$ m. Note that values for all atoms should be approximately equal, so that which atom is used does not matter (if that is not the case, the computation should not be considered to be well-converged). The density at the nucleus only was found under the line "DENSITY AT NUCLEUS", and the labels :RUP and :RDN. For one of the atoms (which again should be approximately equal) the value under TOTAL for :RDN was subtracted for that of :RUP. The density in SI-units is given by

$$\rho_s = \frac{\rho_s [1/a_0^3] \hbar}{(5.2917725 \cdot 10^{-11})^3}. \quad (3.8)$$

Having obtained the spin density, the isotropic HFI parameter, was computed using Equation (2.76), giving the parameter in Joule. The values used for the other parameters were $\mu_B = 9.27400999457 \cdot 10^{-24}$ J T⁻¹, $\mu_0 = 1.25663706 \cdot 10^{-6}$ m kg s⁻² A⁻², $\gamma_{Si} = -53.190 \cdot 10^6$ rad s⁻¹ T⁻¹. Linear regression was performed³ to obtain a value of a which depends on the number of atoms in the supercell, N . Note that due to the negative sign of γ , the value of a is negative, but we report the absolute value. Convergence tests of ρ_s and a with respect to the number of k -points used were performed for all supercell sizes, both for the density at the nucleus and around the Thomson radius.

The a parameter was also computed using the mBJ potential with the original parameterization for the number of k -points deemed necessary by the convergence tests, with the procedure used shown in Appendix A.6.

η was computed for both the PBE and mBJ XC-potentials, using the volume of the different supercell sizes found from the label :VOL in `case.scf`.

³The function `stats.linregress` from the library SciPy[57] for Python was used to perform the linear regression.

3.4 Isotropic Hyperfine Interaction in a Silicon Quantum Dot

After having obtained a linear regression for the hyperfine parameters, the total hyperfine interaction for a QD where every nucleus has a spin and is completely polarized was found, from $a_{total} = 2a_2$. The value was used to compute the random Overhauser field for silicon QDs with various amounts of the finite-spin isotope ^{29}Si .

3.5 Visualizing the Spin-Density

By placing the electron in the conduction band as explained in Section 3.3 the spin-density was plotted in two different planes using LAPW5 by running `x lapw5 -up` with the input files shown in Appendix B.4.

Chapter 4

Results

4.1 Bulk Silicon

Using the PBA XC-functional, a convergence test for the number of k -points in the IBZ (not the total BZ) was performed with $R_{mt}K_{max} = 7.0$ (the default value). The results are shown in Figure 4.1a. The number of k -points satisfying a maximum total energy change of $\Delta E = 0.0001$ Ry, was determined to be 59, as 102 points gave the same energy up to 0.0001 Ry. In addition, a convergence test for $R_{mt}K_{max}$ with respect to the total energy was performed, using a k -mesh of 59 points, as shown in Figure 4.1b, so that the value of $R_{mt}K_{max} = 7.0$ (which is also the default) was chosen for further computations.

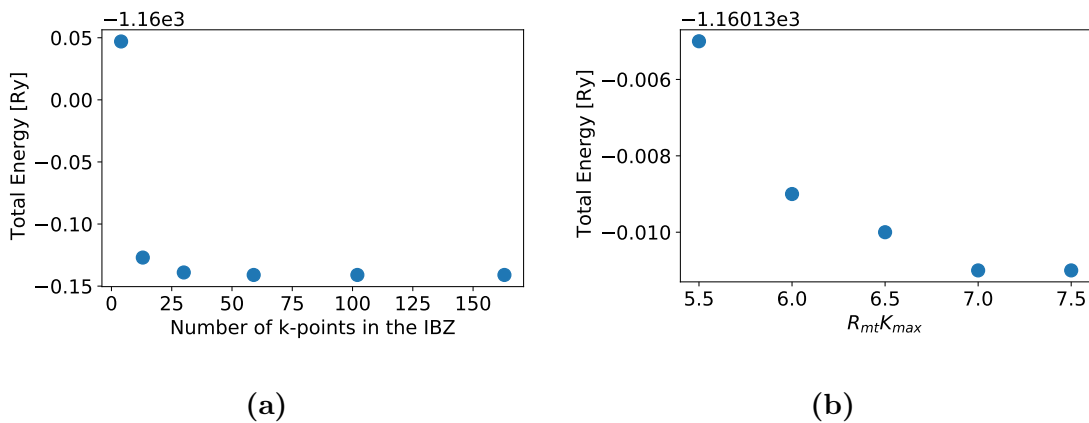


Figure 4.1: a) Total energy with respect to the number of k -points in the IBZ. b) Total energy with respect to $R_{mt}K_{max}$.

The band structure of the cell is shown in Figure 4.2, for a computation with

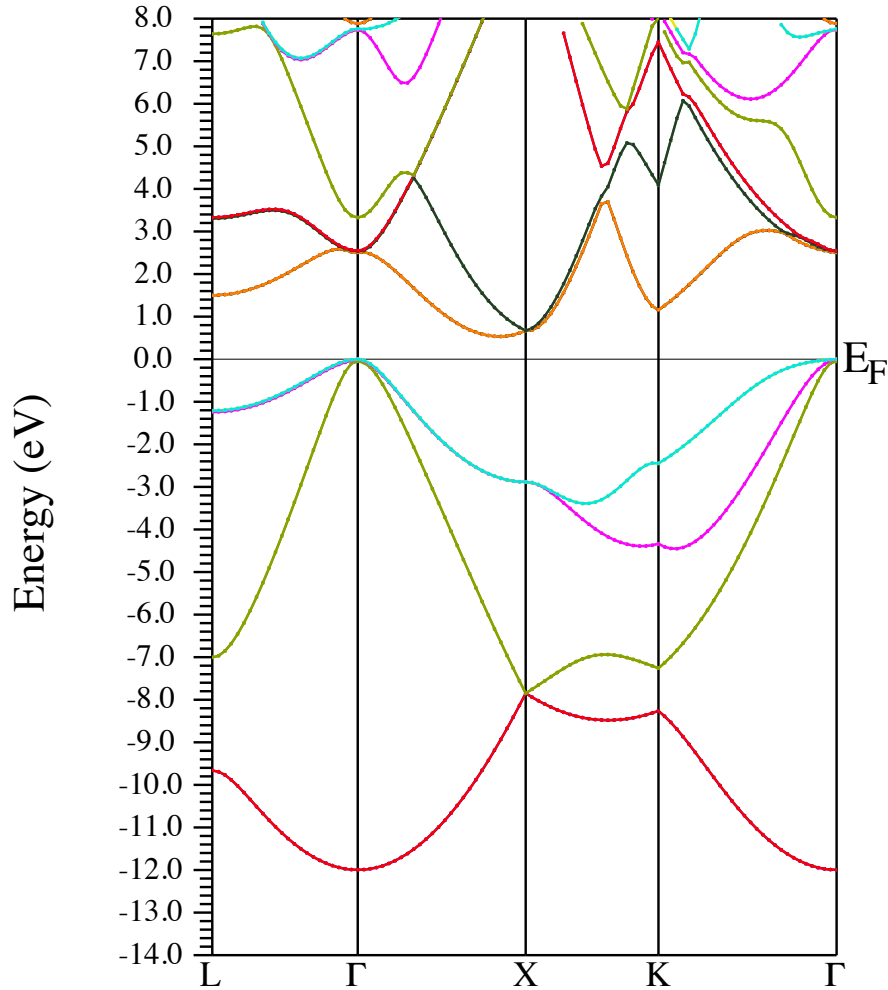


Figure 4.2: Band structure of Si for a computation with 59 k -points and $R_{mt}K_{max} = 7.0$ using the PBE XC-potential with an energy convergence of 0.001 Ry. The band structure is shifted so that E_F is at zero.

59 k -points and $R_{mt}K_{max} = 7.0$. Giving a Fermi energy of 0.386 Ry and a bandgap of 0.559 eV. The conduction band minima was found to be at $\mathbf{k} = (0.77778, 0, 0)$ when using 59 k -points, which is one of the six minima due to symmetry. To precisely determine the conduction band minima, a computation without SOC was performed with 4735 k -points in the IBZ, for which the minima was found to be at $\mathbf{k} = (0.82759, 0, 0)$.

A computation using the LDA XC-potential gave a band gap of 0.482 eV, while using the mBJ potential with Koller parametrization gave a value of 1.126 eV.

4.2 Isotropic Hyperfine Parameter for Silicon Supercells

When determining the k -point of the conduction band minima, the minimum energy of the conduction band, $E_{min} = 0.4249172$ Ry for the spin-up case, was found for the 10 k -values between $k_z = 0.1594$ and $k_z = 0.1585$. The k -point chosen was the average of the largest and smallest k_z which gave the minima, $\mathbf{k} = (0, 0, 0.1589)$. The conduction band minima for the spin-down case was found to have an energy of 0.4251458 Ry, with four k -points having the eigenvalue, from $k_z = 0.1587$ to $k_z = 0.1591$, giving the same average as for the spin-up case. Therefore, $\mathbf{k} = (0, 0, 0.1589)$ was used as the k -value of the conduction band minima.

Convergence tests for the parameters a and a_{r_T} (using the spin-density over the Thomson radius), were performed for all supercell sizes and are shown in Figure D.1 in Appendix D. To achieve a precision of $\Delta a = 0.01$, the convergence tests determined the number of k -points used for the supercells to be $k_N = 125, 40, 32, 14, 8$ for $N = 8, 16, 32, 54, 64$ respectively.

The results of the computed contact interaction, a , and a_{r_T} , along with the corresponding densities using the PBE XC-potential for all supercell sizes, are presented in Table 4.1. For the 64-atom supercell, it was not possible to separate the two lowest-lying conduction bands in LAPW2 due to the energy values being very similar, so that in this case, the two lowest-lying bands were occupied.

For the PBE XC-potential, using linear regression with respect to $1/N$, the slope for a was found to be $4.3\mu\text{eV}$ with a standard deviation of $\sigma = 0.14$. For a_{r_T} the slope was found to be $4.1\mu\text{eV}$ with a standard deviation of $\sigma = 0.13$. The regression was performed without including the results for the 64-atom supercell due to the issue with placing the electron. The computed values of a and a_{r_T} along with the interpolation and the 64-atom point with its computed value divided by two is shown in Figure 4.3.

The computed hyperfine parameters using the mBJ XC-potential are shown in Table 4.2. Using linear regression with respect to $1/N$ for the values computed with the mBJ potential, the slope for a was found to be $4.0\mu\text{eV}$ with a standard deviation of $\sigma = 0.1$. For a_{r_T} the slope was found to be $3.8\mu\text{eV}$ with a standard deviation

Table 4.1: Computed hyperfine parameters a and a_{r_T} using the PBE XC-potential, where N is the number of atoms in the supercell, ρ_s is the spin-density at the nucleus, ρ_{s,r_T} is the spin-density averaged over the Thomson radius (corresponding to a_{r_T}), k_N is the number of k -points used in the computation, and a_{Assali} are the values obtained from the interpolation by Assali *et al.*[14]. Note that for the 64-atom supercell the two lowest-lying conduction bands are occupied instead of only the lowest-lying conduction band.

N	k_N	ρ_{s,r_T}	a_{r_T}	ρ_s	a	a_{Assali}
8	125	0.142 a_0^{-3}	$0.52 \mu\text{eV}$	0.147 a_0^{-3}	$0.54 \mu\text{eV}$	$0.54 \mu\text{eV}$
16	40	0.074 a_0^{-3}	$0.27 \mu\text{eV}$	0.076 a_0^{-3}	$0.28 \mu\text{eV}$	$0.27 \mu\text{eV}$
32	32	0.037 a_0^{-3}	$0.14 \mu\text{eV}$	0.038 a_0^{-3}	$0.14 \mu\text{eV}$	$0.13 \mu\text{eV}$
54	14	0.021 a_0^{-3}	$0.08 \mu\text{eV}$	0.022 a_0^{-3}	$0.08 \mu\text{eV}$	$0.08 \mu\text{eV}$
64	8	0.037 a_0^{-3}	$0.14 \mu\text{eV}$	0.038 a_0^{-3}	$0.14 \mu\text{eV}$	$0.07 \mu\text{eV}$

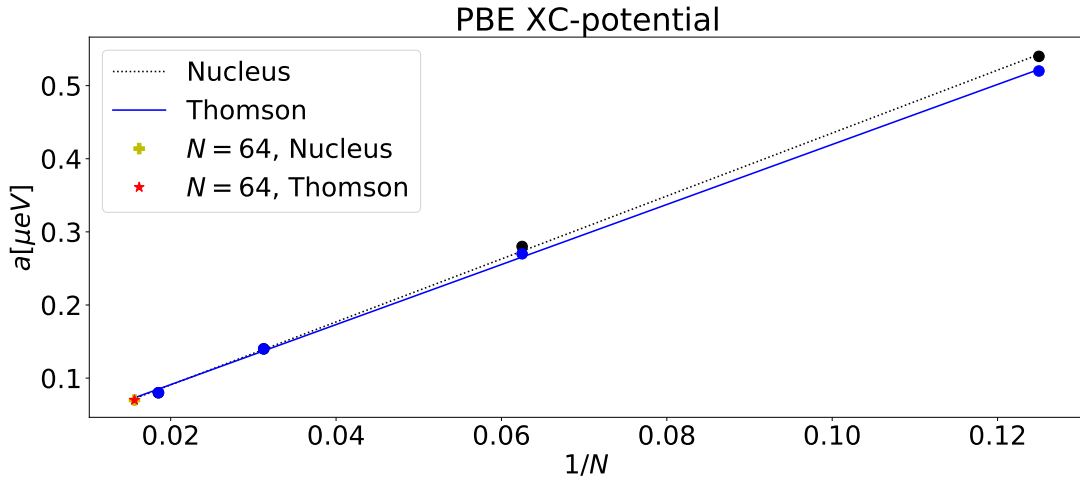


Figure 4.3: Computed values of a and a_{r_T} as a function of $1/N$ together with the interpolated values using the PBE XC-potential. The dotted black line and dots show the interpolation and computed values respectively when using the density at the nucleus. The blue line and dots show the interpolation and computed values when using the average density over the Thomson radius. The yellow cross shows the computed value using the density of the nucleus when using the computed value for $N = 64$ divided by two. The red star shows the same when using the density over the Thomson radius.

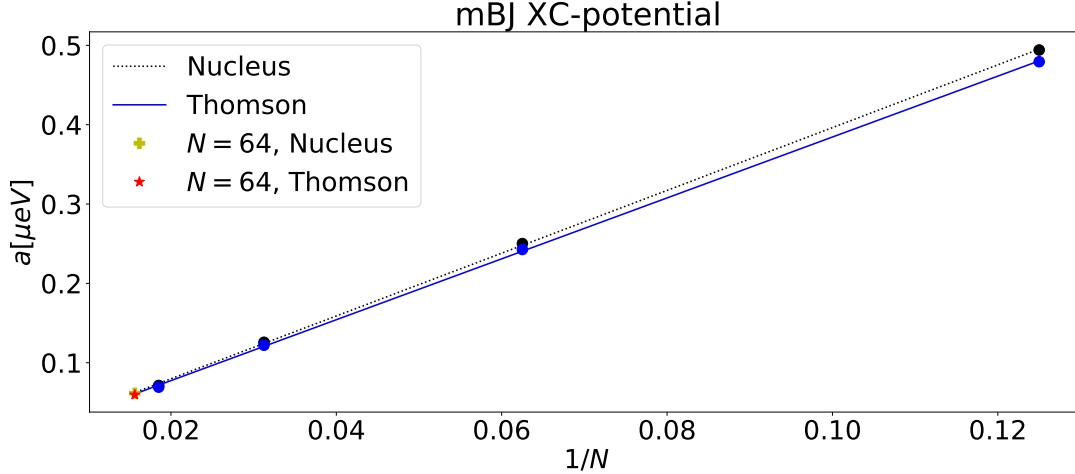


Figure 4.4: Computed values of a and a_{r_T} as a function of $1/N$ together with the interpolated values using the mBJ XC-potential. The blue line and dots show the interpolation and computed values when using the average density over the Thomson radius. The yellow cross shows the computed value using the density of the nucleus when using the computed value for $N = 64$ divided by two. The red star shows the same for average density over the Thomson radius.

of $\sigma = 0.1$. The regression was also, in this case, performed without including the results for the 64-atom supercell. The computed values of a and a_{r_T} along with the interpolation and the 64-atom point with its computed value divided by two is shown in Figure 4.3. The linear interpolations for all cases are summarized in Table 4.3.

The computed values of η for the PBE and mBJ potentials for both ρ_s and ρ_{s,r_T} for the different supercell sizes is shown in Figure 4.5. The volumes of the supercells were found to be $\Omega = [1080.42995, 2160.85984, 4324.10352, 7292.92402, 8643.4396]$. The average values for each case with error are shown in Table 4.4.

4.3 Isotropic Hyperfine Parameter for a Silicon Quantum Dot

Using the linear regression for a primitive unit cell (with $N = 2$) using the computed value for a_{r_T} for the mBJ potential, the value of $a_2 = 1.9 \mu\text{eV}$ was found. Giving

Table 4.2: Computed hyperfine parameters a where N is the number of atoms in the supercell, using the mBJ potential.

N	a	a_{r_T}
8	$0.49 \mu\text{eV}$	$0.48 \mu\text{eV}$
16	$0.25 \mu\text{eV}$	$0.24 \mu\text{eV}$
32	$0.13 \mu\text{eV}$	$0.12 \mu\text{eV}$
54	$0.08 \mu\text{eV}$	$0.08 \mu\text{eV}$
64	$0.06 \mu\text{eV}$	$0.06 \mu\text{eV}$

Table 4.3: Slope of the linear interpolation, such that the value for a supercell containing N atoms is x/N , with $x = a, a_{r_T}$ for the PBE and mBJ-XC potentials.

PBE		mBJ	
a	a_{r_T}	a	a_{r_T}
$4.3 \mu\text{eV}$	$4.1 \mu\text{eV}$	$4.0 \mu\text{eV}$	$3.8 \mu\text{eV}$

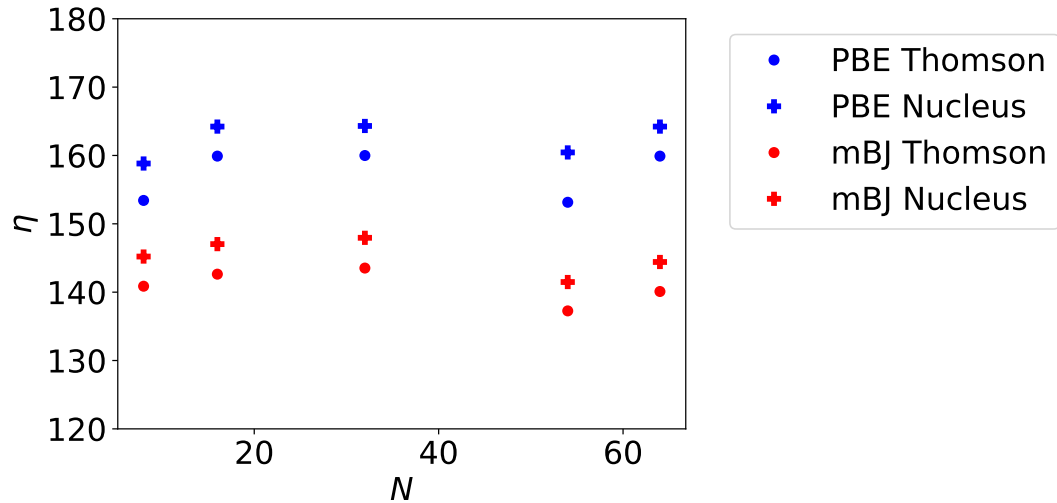


Figure 4.5: Computed values of η for both the PBE and mBJ XC-potentials using the density computed at the nucleus and the average over the Thomson radius.

Table 4.4: Computed values of η for the PBE and mBJ potentials for both ρ_s and ρ_{s,r_T} .

Method	η
PBE, ρ_s	161.5 ± 2.7
PBE, ρ_{s,r_T}	156.5 ± 3.4
mBJ, ρ_s	144.7 ± 3.2
mBJ, ρ_{s,r_T}	140.4 ± 3.1

$a_{total} = 3.8 \mu\text{eV}$ for a QD where all nuclei has finite spin. Considering natural Si, with approximately 5% being ^{29}Si , a_{total} is multiplied by 0.05, to obtain the total HFI giving $a_{natural,total} = 0.19 \mu\text{eV}$. Assuming a QD with a total of 10^5 nuclei, natural silicon has $N_s = 5000$ ^{29}Si nuclei. The random Overhauser field is in this case $\delta A = 2.7 \text{ neV}$, giving $T_2^* = 0.25 \mu\text{s}$. For a QD with 0.08% of the ^{29}Si isotope the computed dephasing time was $T_2^* = 2.5 \mu\text{s}$.

4.4 Visualizing the Spin-Density

The spin-density for an 8-atom supercell in a (100) plane for a state at $\mathbf{k} = (0, 0, 0.1589)$ and placing the electron in the conduction band is shown in Figure 4.6b. The spin density was also computed in a plane perpendicular to the [100] and [011] direction, shown in Figure 4.6a.

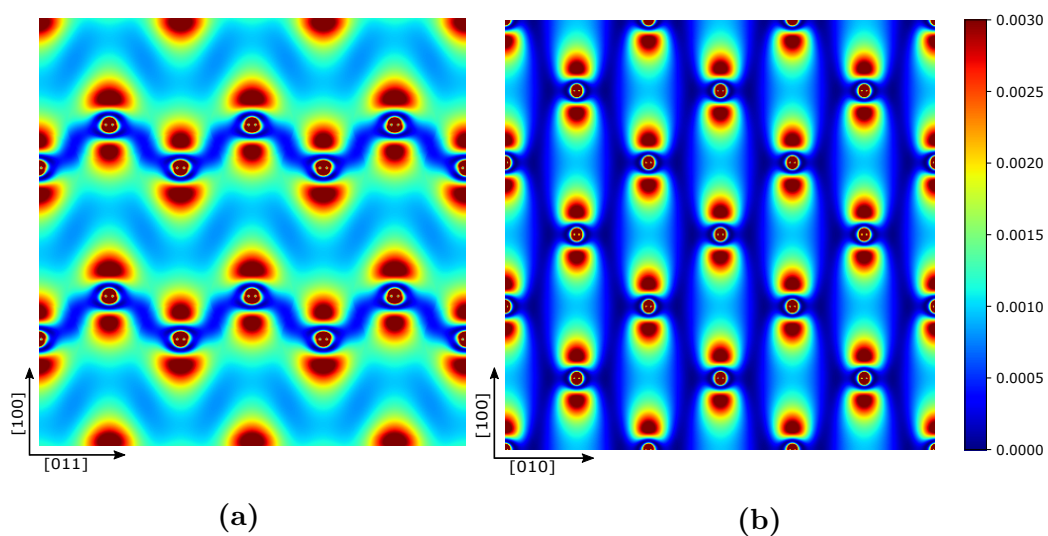


Figure 4.6: Electron spin density, in atomic units, for an electron in the conduction band, n , at the minima at $\mathbf{k} = (0, 0, 0.1589)$. Red are the high density areas, and blue are low density. The high density circular points are the silicon nuclei, where the density is higher than the value indicated by the colour. **a)** Spin density in a plane spanned by the [100] and [011] direction. **b)** Spin density in a (100) direction.

Chapter 5

Discussion

The computed band structure for a primitive silicon cell, compared to the experimentally obtained band structure of silicon[58] looks qualitatively the same. Observe that there is an energy range where no bands exist, identifying the bandgap. In addition, this gap exists at the Fermi energy, E_F , confirming that silicon is indeed a semiconductor. Using the PBE XC-potential the value of the bandgap is underestimated by 51% compared to an experimentally obtained value of $E_g = 1.17$ eV (at $T = 0$ K)[59]. The mBJ potential also gives a smaller value, but only by 1%, indicating that this potential is a better approximation for computations involving the bandgap. It also emphasizes the importance of selecting an appropriate XC-potential for the computation at hand. The conduction band minima were found to be at a lower value than expected. This is due to only including 54 k -points in the mesh, as adding more points gave a more accurate value.

The results achieved using the PBE functional with the spin density taken at the nucleus gave a scaling equal to that of Ref. [14], while the density averaged over the Thomson radius gave a higher value. As taking the density only at the nucleus ignores relativistic effects, the value computed for the Thomson radius is expected to be the most accurate. With the mBJ potential, the density was found to be around $0.3 \mu\text{eV}$ lower than the equivalent case for PBE. The value of a was found, for both mBJ and PBE, to be higher when using the density around the Thomson radius compared to only using the density at the nucleus. It is unclear whether Ref.

[14] uses the Thomson radius approach or only the spin density at the nucleus¹, but as they obtained a slope of $4.3 \mu\text{eV}$, which is in line with our results achieved using PBE when neglecting the finite Thomson radius, it appears as they only used the density at the nucleus.

The difference between the values computed using PBE and mBJ emphasizes the importance of using an appropriate XC-potential in DFT computations. As the mBJ potential gives a more accurate bandgap value, the KS-orbitals computed are likely better estimated and thus better estimate the spin-density.

When expressing the hyperfine interaction tensor through the two parameters, using only the spin-density, the nuclear-orbital interaction, H_L , was neglected. Including the nuclear-orbital interaction requires knowledge of the phase of the wave function. A possibility for including all terms in the HFI is to use the KS-orbitals directly and approximate the Bloch function from these. However, with WIEN2k obtaining the KS-orbitals are somewhat challenging, as the output files only give the parameters from which the orbitals must be reconstructed. If the orbital-nuclear interaction is included, it will lead to an additional anisotropic tensor (which is not traceless) contributing to Equation (2.75). If one considers a system that does not necessarily have axial symmetry, the tensor can give contributions to both the isotropic term, a and the tensor $\tilde{\mathbf{B}}$. In addition, when deriving the Fermi contact contribution, only s -type orbitals were assumed to contribute. In Figure 4.6 the density close to the nucleus is seen to be mainly isotropic, but also some $|p_z\rangle$ character. Only including s -states in the Fermi contact contribution can be justified, and the nuclear-orbital term will likely be small.

Zhao *et al.*[26] has reported a silicon QD which was isotopically purified to 800 ppm (0.08%) of the ^{29}Si isotope. They found a decoherence time of $T_2^* = 1.4 \mu\text{s}$ with an applied field of 150 mT. The result from the computations performed here gave a decoherence time (from only the isotropic interaction) of $2.5 \mu\text{s}$ (mBJ using Thomson radius) for a case of ^{29}Si . The experimentally obtained value is lower than the values computed in this work, which is expected due to not including the anisotropic term, assuming an axially symmetric system (which may not be

¹Ref. [14] states that the Fermi density is proportional to the spin density at the nuclear site. However, when discussing the method used, they also refer to the Appendix of an article by Larico *et al.*[60] that includes the contribution around the Thomson radius.

the case for a physical system) which neglects terms in the HFI tensor, along with neglecting the nuclear-orbital interaction. However, based on the results, the s -type orbitals from the isotropic hyperfine interaction significantly contribute to the overall decoherence time of silicon QDs.

The value for the 64-atom supercell was not included in the linear interpolation due to limitations in LAPW2 in terms of precision used in order to determine the occupied bands. However, as these bands have a similar energy eigenvalue, the KS-orbitals for these states are likely similar. Thus, it is reasonable to assume that the lowest-lying conduction band electron contributes around half of the value of the spin-density. We, therefore, estimated the values for the supercell by dividing the computed values by two, which gave values similar to the values computed using linear interpolation.

In the present work, we have assumed that the KS-orbitals can approximate the Bloch function at the k -value of the conduction band minima. The KS-eigenvalues are used to compute the density, which is the exact density solving the SCF (for the given XC-potential). Then the density is identified with the absolute value squared of the Bloch function at the k -point minima from that $\rho_s = 0$ in neutral silicon, $|\phi_n^\uparrow(\mathbf{r})|^2 - |\phi_n^\downarrow(\mathbf{r})|^2 \rightarrow |\Psi_{k_z}(\mathbf{r})|^2$. However, these are not necessarily the same, and as it is the actual underlying Bloch function which is defined in Equation (2.76), the accuracy of the Bloch function is significant when computing the parameter.

Comparing the results obtained with theoretical and experimental values is challenging as various values of η from 88 to over 300 have been reported depending on the method used. A comparison of experimental and theoretical investigations is shown in Table 5.1. Philippopoulos *et al.*[61] computed η for conduction electrons in silicon using the program ELK with the PBE XC-potential, where they, in addition, used $\mathbf{k} \cdot \mathbf{p}$ theory to obtain approximated Bloch functions at the conduction-band minima (only including s -like orbitals). They argued the placement of the conduction band minima at finite k leads to the KS-orbitals (and thus the spin-density) not giving an accurate approximation of the Bloch function, and therefore utilizes $\mathbf{k} \cdot \mathbf{p}$ theory with the KS-orbitals at Γ . With this method, they obtained a value of $\eta = 88$.

Table 5.1: Values of the parameter η obtained experimentally and theoretically using different methods.

Method	η
Present work using mBJ and the Thomson radius	140.4 ± 3.1
DFT using PBE and density at nucleus[14]	159.4 ± 4.5
DFT with k at Γ and $\mathbf{k} \cdot \mathbf{p}$ [61]	88
NMR experiments[38] with an error corrected by Ref. [62]	178 ± 31
NMR experiments[38], corrected by Ref. [61] based on Ref. [63]	132 ± 13
Extrapolating Overhauser shift data[64]	≥ 300
Korringa-relaxation-rate and Knight-shift measurements[65]	100 ± 10

Chapter 6

Conclusions

We have computed the hyperfine parameters a and b for silicon supercells with 8, 16, 32, 54, and 64 atoms using density functional theory as implemented in WIEN2k, using the PBE and mBJ XC-potentials. The computations were performed by first obtaining the total potential for a charged supercell containing one extra electron, and then only using the k -point in the minima, found to be at $\mathbf{k} = (0, 0, 0.1589)$. Further, the electron was constrained to be placed in the conduction band minima of the spin-up state.

The hyperfine parameters were found to scale inversely with the supercell size, and by linear interpolation, the values were found to be $a = 4.3/N\mu\text{eV}$ when using the density at the nucleus and $a_{r_T} = 4.1/N\mu\text{eV}$ when using the average density around the Thomson radius for the PBE functional. The result when using the PBE functional and the density at the nucleus was thus found to agree with the result reported in Ref. [14]. Using the mBJ functional the values found were $a = 3.9/N\mu\text{eV}$ and $a_{r_T} = 3.8/N\mu\text{eV}$. The decoherence time for a quantum dot in natural silicon was found to be $T_2^* = 0.25\ \mu\text{s}$ when using the mBJ functional and using the density around the Thomson radius.

6.1 Further Work

The anisotropic HFI parameter can be computed from the integral in its definition. The spin-density in three dimensions can be obtained by, e.g., using the program `3ddens` in WIEN2k. Further, an integral over the spin-density multiplied by the

factor $\frac{3\cos^2\theta-1}{r^3}$ must be computed. As the integral scales with $1/r^3$, densities closer to the nucleus will give the most significant contributions. After obtaining b , it can be used in order to compute the anisotropic contribution in a quantum dot, as was done in Ref. [14]. Computing the parameter in a physical quantum dot would require numerical estimations of the envelope function.

It would also be interesting to perform the computations using different XC-potentials, as we here demonstrated that a different value of a was obtained using mBJ.

It is also difficult to assess the estimated value of η in light of other computed values for the parameter, and it would be very interesting to look further into how the different estimates were computed.

Bibliography

1. Shor, P. W. Polynomial-Time Algorithms for Prime Factorization and Discrete Logarithms on a Quantum Computer. *SIAM Journal on Computing* **26**, 1484–1509 (1997).
2. Arute, F. *et al.* Quantum supremacy using a programmable superconducting processor. *Nature* **574**, 505–510 (2019).
3. Bruzewicz, C. D., Chiaverini, J., McConnell, R. & Sage, J. M. Trapped-ion quantum computing: Progress and challenges. *Applied Physics Reviews* **6**, 021314 (2019).
4. He, Y. *et al.* A two-qubit gate between phosphorus donor electrons in silicon. *Nature* **571**, 371–375 (2019).
5. Loss, D. & DiVincenzo, D. P. Quantum computation with quantum dots. *Physical Review A* **57**, 120 (1998).
6. Yang, C. H. *et al.* Operation of a silicon quantum processor unit cell above one kelvin. *Nature* **580**, 350–354 (2020).
7. Petit, L. *et al.* Universal quantum logic in hot silicon qubits. *Nature* **580**, 355–359 (2020).
8. Yoneda, J. *et al.* A quantum-dot spin qubit with coherence limited by charge noise and fidelity higher than 99.9%. *Nature Nanotechnology* **13**, 102–106 (2018).
9. Zajac, D. M. *et al.* Resonantly driven CNOT gate for electron spins. *Science* **359**, 439–442 (2018).
10. Mi, X. *et al.* A coherent spin–photon interface in silicon. *Nature* **555**, 599–603 (2018).

11. DiVincenzo, D. P. The Physical Implementation of Quantum Computation. *Fortschritte der Physik* **48**, 771–783 (2000).
12. Paget, D. Optical detection of NMR in high-purity GaAs: Direct study of the relaxation of nuclei close to shallow donors. *Physical Review B* **25**, 4444 (1982).
13. Tyryshkin, A. *et al.* Coherence of spin qubits in silicon. *Journal of Physics: Condensed Matter* **18**, S783 (2006).
14. Assali, L. V. C. *et al.* Hyperfine interactions in silicon quantum dots. *Physical Review B* **83**, 165301 (2011).
15. Hensen, B. *et al.* A silicon quantum-dot-coupled nuclear spin qubit. *Nature Nanotechnology* **15**, 13–17 (2020).
16. Blaha, P., Schwarz, K., Madsen, G., Kvasnicka, D. & Luitz, J. *WIEN2k, An Augmented Plane Wave + Local Orbitals Program for Calculating Crystal Properties* ISBN: 3-9501031-1-2 (Karlheinz Schwarz, Techn. Universität Wien, Austria, 2018).
17. Feynman, R. P. Simulating physics with computers. *International Journal of Theoretical Physics* **21**, 467–488 (1982).
18. Deutsch, D. Quantum theory, the Church-Turing principle and the universal quantum computer. *Proceedings of the Royal Society of London A* **400**, 97–117 (1985).
19. Nielsen, M. A. & Chuang, I. L. *Quantum computation and quantum information* 10th anniversary ed. (Cambridge University Press, 2010).
20. Adamowski, J., law Bednarek, S. & Iomiej Szafran, B. Quantum Computing with Quantum Dots. *Schedae Informaticae* **14** (2005).
21. Vandersypen, L. M. K. & Chuang, I. L. NMR techniques for quantum control and computation. *Reviews of Modern Physics* **76**, 1037–1069 (2005).
22. Tanenbaum, A. & Austin, T. *Structured Computer Organization* 6th edition (Pearson Education Limited, 2013).
23. Hanson, R., Kouwenhoven, L. P., Petta, J. R., Tarucha, S. & Vandersypen, L. M. Spins in few-electron quantum dots. *Reviews of Modern Physics* **79**, 1217 (2007).

24. Shor, P. W. Scheme for reducing decoherence in quantum computer memory. *Physical Review A* **52**, R2493 (1995).
25. Grover, L. K. *A fast quantum mechanical algorithm for database search* in *Proceedings of the twenty-eighth annual ACM symposium on Theory of computing* (1996), 212–219.
26. Zhao, R. *et al.* Single-spin qubits in isotopically enriched silicon at low magnetic field. *Nature Communications* **10**, 1–9 (2019).
27. Golovach, V. N., Borhani, M. & Loss, D. Electric-dipole-induced spin resonance in quantum dots. *Physical Review B* **74**, 165319 (2006).
28. Tokura, Y., van der Wiel, W. G., Obata, T. & Tarucha, S. Coherent single electron spin control in a slanting Zeeman field. *Physical Review Letters* **96**, 047202 (2006).
29. Kittel, C. *Introduction to Solid State Physics* 8th ed. (Wiley, 2005).
30. Audi, G., Kondev, F. G., Wang, M., Huang, W. & Naimi, S. The NUBASE2016 evaluation of nuclear properties. *Chinese Physics C* **41**, 030001 (2017).
31. Tang, K., Kim, H. S., Ramanayaka, A. N., Simons, D. S. & Pomeroy, J. M. Targeted enrichment of ^{28}Si thin films for quantum computing. *Journal of Physics Communications* **4**, 035006 (2020).
32. Corna, A. *et al.* Electrically driven electron spin resonance mediated by spin–valley–orbit coupling in a silicon quantum dot. *npj Quantum Information* **4**, 1–7 (2018).
33. Goswami, S. *et al.* Controllable valley splitting in silicon quantum devices. *Nature Physics* **3**, 41–45 (2007).
34. Friesen, M. & Coppersmith, S. Theory of valley-orbit coupling in a Si/SiGe quantum dot. *Physical Review B* **81**, 115324 (2010).
35. Maune, B. M. *et al.* Coherent singlet-triplet oscillations in a silicon-based double quantum dot. *Nature* **481**, 344–347 (2012).
36. Weissbluth, M. *Atoms and molecules* (Academic press, 1978).
37. Spaeth, J.-M. Elektronen-Kern-Doppelresonanz-Untersuchung von U_2 -Zentren in Kaliumchlorid. *Zeitschrift für Physik* **192**, 107–141 (1966).

38. Shulman, R. & Wyluda, B. Nuclear magnetic resonance of Si²⁹ in *n*- and *p*-type silicon. *Physical Review* **103**, 1127 (1956).
39. Khaetskii, A. V., Loss, D. & Glazman, L. Electron spin decoherence in quantum dots due to interaction with nuclei. *Physical Review Letters* **88**, 186802 (2002).
40. Singh, D. J. & Nordstrom, L. *Planewaves, Pseudopotentials, and the LAPW method* (Springer Science & Business Media, 2006).
41. Hohenberg, P. & Kohn, W. Inhomogeneous electron gas. *Physical Review* **136**, B864 (1964).
42. Kohn, W. & Sham, L. J. Self-consistent equations including exchange and correlation effects. *Physical Review* **140**, A1133 (1965).
43. Eschrig, H. & Pickett, W. Density functional theory of magnetic systems revisited. *Solid State Communications* **118**, 123–127 (2001).
44. Slater, J. C. Wave functions in a periodic potential. *Physical Review* **51**, 846 (1937).
45. Sjöstedt, E., Nordström, L. & Singh, D. An alternative way of linearizing the augmented plane-wave method. *Solid State Communications* **114**, 15–20 (2000).
46. Koelling, D. & Arbman, G. Use of energy derivative of the radial solution in an augmented plane wave method: application to copper. *Journal of Physics F: Metal Physics* **5**, 2041 (1975).
47. Michalíček, G., Betzinger, M., Friedrich, C. & Blügel, S. Elimination of the linearization error and improved basis-set convergence within the FLAPW method. *Computer Physics Communications* **184**, 2670–2679 (2013).
48. Perdew, J. P., Burke, K. & Ernzerhof, M. Generalized gradient approximation made simple. *Physical Review Letters* **77**, 3865 (1996).
49. Becke, A. D. & Johnson, E. R. A simple effective potential for exchange. *The Journal of Chemical Physics* **124**, 221101 (2006).
50. Tran, F. & Blaha, P. Accurate band gaps of semiconductors and insulators with a semilocal exchange-correlation potential. *Physical Review Letters* **102**, 226401 (2009).

51. Koller, D., Tran, F. & Blaha, P. Improving the modified Becke-Johnson exchange potential. *Physical Review B* **85**, 155109 (2012).
52. *User's Guide, WIEN2k 21.1 (Release 04/30/2021)(Downloaded 01.07.2021)* http://www.wien2k.at/reg_user/textbooks/usersguide.pdf.
53. *Calculation of spin-orbit coupling, P. Novák (downloaded 01.07.2021)* http://www.wien2k.at/reg_user/textbooks/novak_lecture_on_spinorbit.pdf.
54. Momma, K. & Izumi, F. VESTA 3 for three-dimensional visualization of crystal, volumetric and morphology data. *Journal of Applied Crystallography* **44**, 1272–1276 (2011).
55. *Calculation of hyperfine field in WIEN2k. Technical Report, P. Novák (Downloaded 14.07.21)* http://www.wien2k.at/reg_user/textbooks/Bhf_3.pdf.
56. Monkhorst, H. J. & Pack, J. D. Special points for Brillouin-zone integrations. *Physical Review B* **13**, 5188 (1976).
57. Virtanen, P. *et al.* SciPy 1.0: Fundamental Algorithms for Scientific Computing in Python. *Nature Methods* **17**, 261–272 (2020).
58. Thurner, G. C. & Debbage, P. Molecular imaging with nanoparticles: the dwarf actors revisited 10 years later. *Histochemistry and Cell Biology* **150**, 733–794 (2018).
59. Ashcroft, N. W. & Mermin, N. D. *Solid state physics* (1976).
60. Larico, R., Justo, J., Machado, W. & Assali, L. Electronic properties and hyperfine fields of nickel-related complexes in diamond. *Physical Review B* **79**, 115202 (2009).
61. Philippopoulos, P., Chesi, S. & Coish, W. First-principles hyperfine tensors for electrons and holes in GaAs and silicon. *Physical Review B* **101**, 115302 (2020).
62. Wilson, D. Electron spin resonance experiments on shallow donors in germanium. *Physical Review* **134**, A265 (1964).
63. Abragam, A. *The principles of nuclear magnetism* **32** (Oxford university press, 1983).

64. Dyakonov, V. & Denninger, G. Overhauser-shift measurements on Si: P near the metal-insulator transition. *Physical Review B* **46**, 5008 (1992).
65. Sundfors, R. & Holcomb, D. Nuclear magnetic resonance studies of the metallic transition in doped silicon. *Physical Review* **136**, A810 (1964).

Appendices

Appendix A

Details of the Computations

The necessary input files needed to be defined by the user, and details of the computation of bulk silicon are presented in this appendix.

A.1 Structure File for Silicon

The structure file for a regular silicon structure can be created using `makestruct.lapw` and choosing to specify the space group, `Fd-3m`. The lattice parameters entered were $a = 5.43 \text{ \AA}$, and angles were 90 degrees. The number of inequivalent atoms was set to 1, and the element Si, at position $(1/8, 1/8, 1/8)$. The corresponding structure file achieved is shown below. Note that the file name must be changed from `init.struct` to `case.struct` before initializing a computation.

```
Si
F  LATTICE,NONEQUIV.ATOMS:  1
MODE OF CALC=RELA unit=bohr
 10.261217 10.261217 10.261217 90.000000 90.000000 90.000000
ATOM  1: X=0.12500000 Y=0.12500000 Z=0.12500000
      MULT= 2          ISPLIT= 0
      1: X=0.87500000 Y=0.87500000 Z=0.87500000
Si      NPT= 781  R0=0.00010000 RMT= 2.21          Z: 14.0
LOCAL ROT MATRIX:  1.0000000 0.0000000 0.0000000
                   0.0000000 1.0000000 0.0000000
                   0.0000000 0.0000000 1.0000000
0 SYMMETRY OPERATIONS:
```

A.2 Numerical Procedure for Bulk Silicon

A spin-polarized calculation, including spin-orbit coupling, using the PBE XC-potential for bulk silicon using the structure in Appendix A.1 was performed. The procedure used is shown in the text below.

Running `init_so_lapw` helps to create and modify input files (`case.inso`, `case.in1`, `case.in2(c)`) needed for including SOC. When running `init_so_lapw` several inputs are asked for. The program asks for the direction of the moment, where the default value of $(0, 0, 1)$ was chosen. Next, it asks for the number of atoms without SOC, where the default of none was chosen. Then it asks for an increase of EMAX, where the default value of 5.0 Ry was chosen. No RLOs were added. The input results in the file `case.inso` shown in Appendix B. The program asks if this is a spin-polarized case, and yes should be chosen so that `symmetso` is run, which creates new structure files. These files were accepted so that they replaced the old files.

```
init_lapw -b -sp
runsp_lapw

# to save files in a directory
save_lapw -d sp

init_so_lapw
runsp_lapw -so
```

A.3 k -mesh Convergence Test

Convergence of total energy with respect to the k -mesh size was done by running `xkgen` to specify the number of points in the total BZ. A SCF cycle for the produced `case.klist` was performed using the procedure from Appendix A.2, using an energy convergence of 0.0001 Ry, the PBE XC-potential, and $R_{mt}K_{max} = 7.0$. Further, the

total energy for each k -mesh size was obtained from the `:ENE` label in `case.scf`.

A.4 $R_{mt}K_{max}$ Convergence Test

In this case, the computation was initialized with `init_lapw -sp -rkmax X -b`, where X is the $R_{mt}K_{max}$ value which the computation is done for. Then the procedure in Appendix B was used, and running `x kgen` with a total of 59 points in the IBZ.

A.5 Computation Using the mBJ XC-Potential

A procedure for a computation with spin-polarization and SOC using the modified Becke-Johnson potential is shown below.

```
init_lapw -sp -b
runsp_lapw
save_lapw -d PBE

init_so_lapw
runsp_lapw -so

init_mbj_lapw
runsp_lapw -NI -so -i 1
save_lapw -d PBE_so

init_mbj_lapw # select option 1 for Koller parametrization
runsp_lapw -so -i 80
```

One cycle in an SCF computation with spin-polarization and SOC runs the programs with the flags shown below. `x lapw0 -grr` computes the semi-local exchange using the input file `case.in0_grr`. In the case of mBJ it computes the average of $|\nabla\rho|/\rho$, used in LAPW0 to compute the total potential. In LAPW2 the flag `-vresp` is used to create the files `case.vrespval/sum(up/dn)`.

```
x lapw0 -grr
x lapw0
```

```
x lapw1 -up
x lapw1 -dn
x lapwso -up
x lapw2 -up -vresp -c -so
x lapw2 -dn -vresp -c -so
x lcore -up
x lcore -dn
x mixer
x mixer_vresp
```

A.6 Procedure for Computing the Isotropic Hyperfine Interaction

The procedure below was used to obtain the spin-density for a Hamiltonian at a fixed k -value, with an electron placed in the conduction band. The density is then used to compute the isotropic hyperfine interaction, a , for various supercell sizes.

```
# after performing initialization of the supercell
init_lapw -b -sp
runsp_lapw
save_lapw -d sp

init_so_lapw
runsp_lapw -so

save_lapw -d neutral

# change case.inm and case.in2c

runsp_lapw -so

# locate the k-point of the conduction band minima
# and the eigenvalue of the minima X
# and the eigenvalue of the highest conduction band Y
```

```
# do not save computation

x lapw0

# remove all but the conduction band minima in case.klist

x lapw1 -up
x lapw1 -dn

x lapwso -up

x lapw2 -so -up -all -9 X # X should be slightly higher than the minima
x lapw2 -so -dn -all -9 Y # Y should be slightly higher than the conduction band

# check case.output2up/dn to ensure correct occupation

x mixer
```

When using the mBJ potential with the original parameters, the procedure below was used.

```
init_lapw -sp -b
runsp_lapw
save_lapw -d PBE

init_so_lapw
runsp_lapw -so

save_lapw -d neutral

# add charge

runsp_lapw -so

init_mbj_lapw
runsp_lapw -NI -so -i 1 -p

save_lapw PBE_so
```

```
init_mbj_lapw # select option 0
runsp_lapw -so -i 80 -p

# locate the k-point of the conduction band minima
# and the eigenvalue of the minima X
# and the eigenvalue of the highest conduction band Y
# do not save computation

x lapw0 -grr
x lapw0

# remove all but the conduction band minima in case.klist

x lapw1 -up
x lapw1 -dn
x lapwso -up
x lapw2 -up -vresp -c -so -all -9 X
x lapw2 -dn -vresp -c -so -all -9 Y

x mixer
```

A.7 case.output2up/dn

Parts of the `case.output2up/dn` file relevant for determining if the electrons are placed correctly are shown below, in this case for a supercell of $N = 8$ atoms. Note that there are more bands in the files (a total of 75 for the $N = 8$ atom supercell) that are not shown here.

Below is the `case.output2up` file, where the occupation number of all bands up to and including band number 17 (which is the lowest-lying conduction band) is 1.

```
Bandranges emin - emax and occupancy:
band      1  -0.4918399887  -0.4918399887    0.100000D+01  ALL  -9.0000  0.4140
band      2  -0.3049462538  -0.3049462538    0.100000D+01  ALL  -9.0000  0.4140
band      3  -0.1954897277   -0.1954897277    0.100000D+01  ALL  -9.0000  0.4140
```

band	4	-0.1954447647	-0.1954447647	0.100000D+01	ALL	-9.0000	0.4140
band	5	-0.1953568245	-0.1953568245	0.100000D+01	ALL	-9.0000	0.4140
band	6	-0.1953200262	-0.1953200262	0.100000D+01	ALL	-9.0000	0.4140
band	7	-0.0785719530	-0.0785719530	0.100000D+01	ALL	-9.0000	0.4140
band	8	0.1344736312	0.1344736312	0.100000D+01	ALL	-9.0000	0.4140
band	9	0.1345451818	0.1345451818	0.100000D+01	ALL	-9.0000	0.4140
band	10	0.1346145817	0.1346145817	0.100000D+01	ALL	-9.0000	0.4140
band	11	0.1346416640	0.1346416640	0.100000D+01	ALL	-9.0000	0.4140
band	12	0.1770535485	0.1770535485	0.100000D+01	ALL	-9.0000	0.4140
band	13	0.1770958352	0.1770958352	0.100000D+01	ALL	-9.0000	0.4140
band	14	0.3072521264	0.3072521264	0.100000D+01	ALL	-9.0000	0.4140
band	15	0.3336549260	0.3336549260	0.100000D+01	ALL	-9.0000	0.4140
band	16	0.3337060632	0.3337060632	0.100000D+01	ALL	-9.0000	0.4140
band	17	0.4139988349	0.4139988349	0.100000D+01	ALL	-9.0000	0.4140
band	18	0.4675594653	0.4675594653	0.000000D+00			
band	19	0.4865941213	0.4865941213	0.000000D+00			

Below is the case.output2dn file, where the occupation number of all bands up to and including band number 16 (which is the valence band with the highest energy) is 1.

Bandranges emin - emax and occupancy:

band	1	-0.4918337644	-0.4918337644	0.100000D+01	ALL	-9.0000	0.4000
band	2	-0.3049346282	-0.3049346282	0.100000D+01	ALL	-9.0000	0.4000
band	3	-0.1955310722	-0.1955310722	0.100000D+01	ALL	-9.0000	0.4000
band	4	-0.1955121934	-0.1955121934	0.100000D+01	ALL	-9.0000	0.4000
band	5	-0.1952995144	-0.1952995144	0.100000D+01	ALL	-9.0000	0.4000
band	6	-0.1952724152	-0.1952724152	0.100000D+01	ALL	-9.0000	0.4000
band	7	-0.0785456520	-0.0785456520	0.100000D+01	ALL	-9.0000	0.4000
band	8	0.1345463033	0.1345463033	0.100000D+01	ALL	-9.0000	0.4000
band	9	0.1345652068	0.1345652068	0.100000D+01	ALL	-9.0000	0.4000
band	10	0.1346242274	0.1346242274	0.100000D+01	ALL	-9.0000	0.4000
band	11	0.1346875012	0.1346875012	0.100000D+01	ALL	-9.0000	0.4000
band	12	0.1769753831	0.1769753831	0.100000D+01	ALL	-9.0000	0.4000
band	13	0.1770101721	0.1770101721	0.100000D+01	ALL	-9.0000	0.4000
band	14	0.3073499650	0.3073499650	0.100000D+01	ALL	-9.0000	0.4000
band	15	0.3335960679	0.3335960679	0.100000D+01	ALL	-9.0000	0.4000
band	16	0.3336256512	0.3336256512	0.100000D+01	ALL	-9.0000	0.4000

A. Details of the Computations

band	17	0.4141435646	0.4141435646	0.000000D+00
band	18	0.4676977944	0.4676977944	0.000000D+00
band	19	0.4865820227	0.4865820227	0.000000D+00

Appendix B

Input Files

B.1 case.inso

```
WFFIL
4 0 0          llmax, ipr, kpot
-10 1.5       Emin, Emax
  0 0 1              h, k, l direction of magnetization
  0              number of atoms with RLO
0 0            number of atoms without SO, atomnumbers
```

B.2 case.klist_band

```
L          46  46 -46  92  2.0-8.00 8.00    k-list generated by XCrySDen
          44  44 -44  92  2.0
          42  42 -42  92  2.0
          40  40 -40  92  2.0
          38  38 -38  92  2.0
          36  36 -36  92  2.0
          34  34 -34  92  2.0
          32  32 -32  92  2.0
          30  30 -30  92  2.0
          28  28 -28  92  2.0
          26  26 -26  92  2.0
          24  24 -24  92  2.0
```

B. Input Files

	22	22	-22	92	2.0
	20	20	-20	92	2.0
	18	18	-18	92	2.0
	16	16	-16	92	2.0
	14	14	-14	92	2.0
	12	12	-12	92	2.0
	10	10	-10	92	2.0
	8	8	-8	92	2.0
	6	6	-6	92	2.0
	4	4	-4	92	2.0
	2	2	-2	92	2.0
GAMMA	0	0	0	108	2.0
	4	0	0	108	2.0
	8	0	0	108	2.0
	12	0	0	108	2.0
	16	0	0	108	2.0
	20	0	0	108	2.0
	24	0	0	108	2.0
	28	0	0	108	2.0
	32	0	0	108	2.0
	36	0	0	108	2.0
	40	0	0	108	2.0
	44	0	0	108	2.0
	48	0	0	108	2.0
	52	0	0	108	2.0
	56	0	0	108	2.0
	60	0	0	108	2.0
	64	0	0	108	2.0
	68	0	0	108	2.0
	72	0	0	108	2.0
	76	0	0	108	2.0
	80	0	0	108	2.0
	84	0	0	108	2.0
	88	0	0	108	2.0
	92	0	0	108	2.0
	96	0	0	108	2.0
	100	0	0	108	2.0
	104	0	0	108	2.0
X	84	0	0	84	2.0

	83	-3	0	84	2.0
	82	-6	0	84	2.0
	81	-9	0	84	2.0
	80	-12	0	84	2.0
	79	-15	0	84	2.0
	78	-18	0	84	2.0
	77	-21	0	84	2.0
	76	-24	0	84	2.0
	75	-27	0	84	2.0
	74	-30	0	84	2.0
	73	-33	0	84	2.0
	72	-36	0	84	2.0
	71	-39	0	84	2.0
	70	-42	0	84	2.0
	69	-45	0	84	2.0
	68	-48	0	84	2.0
	67	-51	0	84	2.0
	66	-54	0	84	2.0
	65	-57	0	84	2.0
	64	-60	0	84	2.0
K	87	-87	0	116	2.0
	84	-84	0	116	2.0
	81	-81	0	116	2.0
	78	-78	0	116	2.0
	75	-75	0	116	2.0
	72	-72	0	116	2.0
	69	-69	0	116	2.0
	66	-66	0	116	2.0
	63	-63	0	116	2.0
	60	-60	0	116	2.0
	57	-57	0	116	2.0
	54	-54	0	116	2.0
	51	-51	0	116	2.0
	48	-48	0	116	2.0
	45	-45	0	116	2.0
	42	-42	0	116	2.0
	39	-39	0	116	2.0
	36	-36	0	116	2.0
	33	-33	0	116	2.0

```
30 -30 0 116 2.0
27 -27 0 116 2.0
24 -24 0 116 2.0
21 -21 0 116 2.0
18 -18 0 116 2.0
15 -15 0 116 2.0
12 -12 0 116 2.0
9 -9 0 116 2.0
6 -6 0 116 2.0
3 -3 0 116 2.0
GAMMA 0 0 0 116 2.0
END
```

B.3 case.insp

```
### Figure configuration
5.0 3.0 # paper offset of plot
10.0 15.0 # xsize,ysize [cm]
1.0 4 # major ticks, minor ticks
1.0 1 # character height, font switch
1.1 2 4 # line width, line switch, color switch
### Data configuration
-14.0 8.0 2 # energy range, energy switch 1:Ry, 2:eV
1 0.3867 # Fermi switch, Fermi-level in Ry units
1 999 # number of bands for heavier plotting 1,1
0 1 0.2 # jatom, jtype, size of heavier plotting
```

B.4 case.in5

The input file for plotting the spin-density using LAPW5 for a (100) plane of an 8-atom conventional supercell is shown below.

```
0 -10000000 -10000000 10000000
0 20000000 -10000000 10000000
```

```
      0  -10000000  20000000  10000000
3 2 3
100 100
RHO SUB
ATU VAL NODEBUG
NONORTHO
```

The input file for plotting the spin-density in a plane perpendicular to the [100] and [011] directions is shown below.

```
      12500000  -2500000  16250000  10000000
      12500000  -2500000  -8750000  10000000
      -2500000  12500000  16250000  10000000
3 2 3
2000 2000
RHO SUB
ATU VAL NODEBUG
NONORTHO
```

Appendix C

Supercells

All supercells were created using a primitive cell as the unit cell. The supercells were created using VESTA[54] and are visualized in Figure C.1.

C.1 8-atom Supercell

The struct file used for an 8-atom supercell is shown below.

```
Si221F
P LATTICE,NONEQUIV.ATOMS 8 0
MODE OF CALC=RELA unit=bohr
14.514219 14.514219 7.257110 60.000004 60.000004 60.000004
ATOM -1: X=0.00000000 Y=0.00000000 Z=0.00000000
MULT= 1 ISPLIT=15
Si1 NPT= 781 R0=.000100000 RMT= 2.00000 Z: 14.00000
LOCAL ROT MATRIX: 1.0000000 0.0000000 0.0000000
0.0000000 1.0000000 0.0000000
0.0000000 0.0000000 1.0000000
ATOM -2: X=0.12500000 Y=0.12500000 Z=0.25000000
MULT= 1 ISPLIT=15
Si2 NPT= 781 R0=.000100000 RMT= 2.00000 Z: 14.00000
LOCAL ROT MATRIX: 1.0000000 0.0000000 0.0000000
0.0000000 1.0000000 0.0000000
0.0000000 0.0000000 1.0000000
ATOM -3: X=0.12500000 Y=0.62500000 Z=0.25000000
MULT= 1 ISPLIT=15
```

C. Supercells

```
Si3      NPT= 781  R0=.000100000  RMT= 2.00000  Z: 14.00000
LOCAL ROT MATRIX:  1.0000000  0.0000000  0.0000000
                   0.0000000  1.0000000  0.0000000
                   0.0000000  0.0000000  1.0000000
ATOM  -4: X=0.50000000 Y=0.00000000 Z=0.00000000
          MULT= 1          ISPLIT=15
Si4      NPT= 781  R0=.000100000  RMT= 2.00000  Z: 14.00000
LOCAL ROT MATRIX:  1.0000000  0.0000000  0.0000000
                   0.0000000  1.0000000  0.0000000
                   0.0000000  0.0000000  1.0000000
ATOM  -5: X=0.00000000 Y=0.50000000 Z=0.00000000
          MULT= 1          ISPLIT=15
Si5      NPT= 781  R0=.000100000  RMT= 2.00000  Z: 14.00000
LOCAL ROT MATRIX:  1.0000000  0.0000000  0.0000000
                   0.0000000  1.0000000  0.0000000
                   0.0000000  0.0000000  1.0000000
ATOM  -6: X=0.50000000 Y=0.50000000 Z=0.00000000
          MULT= 1          ISPLIT=15
Si6      NPT= 781  R0=.000100000  RMT= 2.00000  Z: 14.00000
LOCAL ROT MATRIX:  1.0000000  0.0000000  0.0000000
                   0.0000000  1.0000000  0.0000000
                   0.0000000  0.0000000  1.0000000
ATOM  -7: X=0.62500000 Y=0.12500000 Z=0.25000000
          MULT= 1          ISPLIT=15
Si7      NPT= 781  R0=.000100000  RMT= 2.00000  Z: 14.00000
LOCAL ROT MATRIX:  1.0000000  0.0000000  0.0000000
                   0.0000000  1.0000000  0.0000000
                   0.0000000  0.0000000  1.0000000
ATOM  -8: X=0.62500000 Y=0.62500000 Z=0.25000000
          MULT= 1          ISPLIT=15
Si8      NPT= 781  R0=.000100000  RMT= 2.00000  Z: 14.00000
LOCAL ROT MATRIX:  1.0000000  0.0000000  0.0000000
                   0.0000000  1.0000000  0.0000000
                   0.0000000  0.0000000  1.0000000

0      NUMBER OF SYMMETRY OPERATIONS
```

C.2 16-atom Supercell

The struct file used for a 16-atom supercell is shown below.

```

Si
P  LATTICE,NONEQUIV.ATOMS  3  0
MODE OF CALC=RELA unit=bohr
  14.514219 14.514219 14.514219 60.000004 60.000004 60.000004
ATOM  -1: X=0.00000000 Y=0.00000000 Z=0.00000000
        MULT=8          ISPLIT=15
      -1: X=0.50000000 Y=0.00000000 Z=0.00000000
      -1: X=0.00000000 Y=0.50000000 Z=0.00000000
      -1: X=0.00000000 Y=0.00000000 Z=0.50000000
      -1: X=0.50000000 Y=0.50000000 Z=0.50000000
      -1: X=0.00000000 Y=0.50000000 Z=0.50000000
      -1: X=0.50000000 Y=0.00000000 Z=0.50000000
      -1: X=0.50000000 Y=0.50000000 Z=0.00000000
Si1      NPT= 781  R0=.000100000 RMT= 2.00000  Z: 14.00000
LOCAL ROT MATRIX:  1.0000000 0.0000000 0.0000000
                   0.0000000 1.0000000 0.0000000
                   0.0000000 0.0000000 1.0000000
ATOM  -2: X=0.12500000 Y=0.12500000 Z=0.12500000
        MULT=7          ISPLIT=15
      -2: X=0.12500000 Y=0.62500000 Z=0.12500000
      -2: X=0.12500000 Y=0.12500000 Z=0.62500000
      -2: X=0.62500000 Y=0.62500000 Z=0.62500000
      -2: X=0.12500000 Y=0.62500000 Z=0.62500000
      -2: X=0.62500000 Y=0.12500000 Z=0.62500000
      -2: X=0.62500000 Y=0.62500000 Z=0.12500000
Si2      NPT= 781  R0=.000100000 RMT= 2.00000  Z: 14.00000
LOCAL ROT MATRIX:  1.0000000 0.0000000 0.0000000
                   0.0000000 1.0000000 0.0000000
                   0.0000000 0.0000000 1.0000000
ATOM  -3: X=0.62500000 Y=0.12500000 Z=0.12500000
        MULT=1          ISPLIT=15
Si3      NPT= 781  R0=.000100000 RMT= 2.00000  Z: 14.00000
LOCAL ROT MATRIX:  1.0000000 0.0000000 0.0000000
                   0.0000000 1.0000000 0.0000000
                   0.0000000 0.0000000 1.0000000

```

C.3 32-atom Supercell

The struct file used for a 32-atom supercell is shown below.

```
Si422F
P LATTICE,NONEQUIV.ATOMS 5 0
MODE OF CALC=RELA unit=bohr
29.028440 14.514219 14.514219 60.000004 60.000004 60.000004
ATOM -1: X=0.00000000 Y=0.00000000 Z=0.00000000
      MULT=13          ISPLIT=15
-1: X=0.25000000 Y=0.00000000 Z=0.00000000
-1: X=0.25000000 Y=0.50000000 Z=0.50000000
-1: X=0.25000000 Y=0.00000000 Z=0.50000000
-1: X=0.25000000 Y=0.50000000 Z=0.00000000
-1: X=0.50000000 Y=0.00000000 Z=0.00000000
-1: X=0.50000000 Y=0.50000000 Z=0.00000000
-1: X=0.50000000 Y=0.00000000 Z=0.50000000
-1: X=0.75000000 Y=0.50000000 Z=0.50000000
-1: X=0.75000000 Y=0.00000000 Z=0.00000000
-1: X=0.75000000 Y=0.50000000 Z=0.00000000
-1: X=0.75000000 Y=0.00000000 Z=0.50000000
-1: X=0.75000000 Y=0.50000000 Z=0.00000000
Si1      NPT= 781 R0=.00010000 RMT= 2.00000 Z: 14.00000
LOCAL ROT MATRIX: 1.0000000 0.0000000 0.0000000
                  0.0000000 1.0000000 0.0000000
                  0.0000000 0.0000000 1.0000000
ATOM -2: X=0.06250000 Y=0.12500000 Z=0.12500000
      MULT=16          ISPLIT=15
-2: X=0.31250000 Y=0.12500000 Z=0.12500000
-2: X=0.06250000 Y=0.62500000 Z=0.12500000
-2: X=0.06250000 Y=0.12500000 Z=0.62500000
-2: X=0.31250000 Y=0.62500000 Z=0.62500000
-2: X=0.56250000 Y=0.62500000 Z=0.62500000
-2: X=0.31250000 Y=0.12500000 Z=0.62500000
-2: X=0.31250000 Y=0.62500000 Z=0.12500000
```

```
-2: X=0.56250000 Y=0.12500000 Z=0.12500000
-2: X=0.81250000 Y=0.12500000 Z=0.12500000
-2: X=0.56250000 Y=0.62500000 Z=0.12500000
-2: X=0.56250000 Y=0.12500000 Z=0.62500000
-2: X=0.81250000 Y=0.62500000 Z=0.62500000
-2: X=0.06250000 Y=0.62500000 Z=0.62500000
-2: X=0.81250000 Y=0.12500000 Z=0.62500000
-2: X=0.81250000 Y=0.62500000 Z=0.12500000
Si2      NPT= 781  R0=.000100000 RMT= 2.00000  Z: 14.00000
LOCAL ROT MATRIX:  1.0000000 0.0000000 0.0000000
                   0.0000000 1.0000000 0.0000000
                   0.0000000 0.0000000 1.0000000
ATOM  -3: X=0.50000000 Y=0.50000000 Z=0.50000000
          MULT=1          ISPLIT=15
Si3      NPT= 781  R0=.000100000 RMT= 2.00000  Z: 14.00000
LOCAL ROT MATRIX:  1.0000000 0.0000000 0.0000000
                   0.0000000 1.0000000 0.0000000
                   0.0000000 0.0000000 1.0000000
ATOM  -4: X=0.00000000 Y=0.00000000 Z=0.50000000
          MULT=1          ISPLIT=15
Si4      NPT= 781  R0=.000100000 RMT= 2.00000  Z: 14.00000
LOCAL ROT MATRIX:  1.0000000 0.0000000 0.0000000
                   0.0000000 1.0000000 0.0000000
                   0.0000000 0.0000000 1.0000000
ATOM  -5: X=0.00000000 Y=0.50000000 Z=0.00000000
          MULT=1          ISPLIT=15
Si5      NPT= 781  R0=.000100000 RMT= 2.00000  Z: 14.00000
LOCAL ROT MATRIX:  1.0000000 0.0000000 0.0000000
                   0.0000000 1.0000000 0.0000000
                   0.0000000 0.0000000 1.0000000
0        NUMBER OF SYMMETRY OPERATIONS
```

C.4 54-atom Supercell

The struct file used for a 54-atom supercell is shown below.

C. Supercells

Si333F

P LATTICE,NONEQUIV.ATOMS 3 1 P1

MODE OF CALC=RELA unit=bohr

21.771329 21.771329 21.771329 60.000000 60.000000 60.000000

ATOM -1: X=0.00000000 Y=0.00000000 Z=0.00000000

MULT=26 ISPLIT=15

-1: X=0.33333333 Y=0.33333333 Z=0.66666667

-1: X=0.66666667 Y=0.66666667 Z=0.33333333

-1: X=0.33333333 Y=0.66666667 Z=0.33333333

-1: X=0.66666667 Y=0.00000000 Z=0.00000000

-1: X=0.00000000 Y=0.33333333 Z=0.66666667

-1: X=0.66666667 Y=0.33333333 Z=0.66666667

-1: X=0.00000000 Y=0.66666667 Z=0.33333333

-1: X=0.33333333 Y=0.00000000 Z=0.00000000

-1: X=0.66666667 Y=0.33333333 Z=0.33333333

-1: X=0.00000000 Y=0.66666667 Z=0.00000000

-1: X=0.33333333 Y=0.00000000 Z=0.66666667

-1: X=0.00000000 Y=0.00000000 Z=0.66666667

-1: X=0.33333333 Y=0.33333333 Z=0.33333333

-1: X=0.66666667 Y=0.66666667 Z=0.00000000

-1: X=0.33333333 Y=0.66666667 Z=0.00000000

-1: X=0.66666667 Y=0.00000000 Z=0.66666667

-1: X=0.00000000 Y=0.33333333 Z=0.33333333

-1: X=0.33333333 Y=0.66666667 Z=0.66666667

-1: X=0.66666667 Y=0.00000000 Z=0.33333333

-1: X=0.00000000 Y=0.33333333 Z=0.00000000

-1: X=0.66666667 Y=0.33333333 Z=0.00000000

-1: X=0.00000000 Y=0.66666667 Z=0.66666667

-1: X=0.00000000 Y=0.00000000 Z=0.33333333

-1: X=0.33333333 Y=0.33333333 Z=0.00000000

-1: X=0.66666667 Y=0.66666667 Z=0.66666667

Si1 NPT= 781 R0=.000100000 RMT= 2.00000 Z: 14.00000

LOCAL ROT MATRIX: 1.0000000 0.0000000 0.0000000

0.0000000 1.0000000 0.0000000

0.0000000 0.0000000 1.0000000

ATOM -2: X=0.08333300 Y=0.08333300 Z=0.08333300

MULT=27 ISPLIT=15

-2: X=0.41666633 Y=0.41666633 Z=0.74999967

```
-2: X=0.74999967 Y=0.74999967 Z=0.41666633
-2: X=0.41666633 Y=0.74999967 Z=0.41666633
-2: X=0.74999967 Y=0.08333300 Z=0.08333300
-2: X=0.08333300 Y=0.41666633 Z=0.74999967
-2: X=0.74999967 Y=0.41666633 Z=0.74999967
-2: X=0.08333300 Y=0.74999967 Z=0.41666633
-2: X=0.41666633 Y=0.08333300 Z=0.08333300
-2: X=0.74999967 Y=0.41666633 Z=0.41666633
-2: X=0.08333300 Y=0.74999967 Z=0.08333300
-2: X=0.41666633 Y=0.08333300 Z=0.74999967
-2: X=0.08333300 Y=0.08333300 Z=0.74999967
-2: X=0.41666633 Y=0.41666633 Z=0.41666633
-2: X=0.74999967 Y=0.74999967 Z=0.08333300
-2: X=0.41666633 Y=0.74999967 Z=0.08333300
-2: X=0.74999967 Y=0.08333300 Z=0.74999967
-2: X=0.08333300 Y=0.41666633 Z=0.41666633
-2: X=0.41666633 Y=0.74999967 Z=0.74999967
-2: X=0.74999967 Y=0.08333300 Z=0.41666633
-2: X=0.08333300 Y=0.41666633 Z=0.08333300
-2: X=0.74999967 Y=0.41666633 Z=0.08333300
-2: X=0.08333300 Y=0.74999967 Z=0.74999967
-2: X=0.41666633 Y=0.08333300 Z=0.41666633
-2: X=0.08333300 Y=0.08333300 Z=0.41666633
-2: X=0.41666633 Y=0.41666633 Z=0.08333300
-2: X=0.74999967 Y=0.74999967 Z=0.74999967
Si2      NPT= 781 R0=.000100000 RMT= 2.00000 Z: 14.00000
LOCAL ROT MATRIX: 1.0000000 0.0000000 0.0000000
                   0.0000000 1.0000000 0.0000000
                   0.0000000 0.0000000 1.0000000
ATOM -3: X=0.33333333 Y=0.00000000 Z=0.33333333
        MULT=1          ISPLIT=15
Si3      NPT= 781 R0=.000100000 RMT= 2.00000 Z: 14.00000
LOCAL ROT MATRIX: 1.0000000 0.0000000 0.0000000
                   0.0000000 1.0000000 0.0000000
                   0.0000000 0.0000000 1.0000000
0        NUMBER OF SYMMETRY OPERATIONS
```

C.5 64-atom Supercell

The struct file used for a 64-atom supercell is shown below.

```
Si442F
P  LATTICE,NONEQUIV.ATOMS  4  0
MODE OF CALC=RELA unit=bohr
 29.028440 29.028440 14.514219 60.000004 60.000004 60.000004
ATOM  -1: X=0.00000000 Y=0.00000000 Z=0.00000000
      MULT=16          ISPLIT=15
      -1: X=0.25000000 Y=0.00000000 Z=0.00000000
      -1: X=0.00000000 Y=0.25000000 Z=0.00000000
      -1: X=0.00000000 Y=0.00000000 Z=0.50000000
      -1: X=0.25000000 Y=0.25000000 Z=0.50000000
      -1: X=0.50000000 Y=0.25000000 Z=0.50000000
      -1: X=0.25000000 Y=0.50000000 Z=0.50000000
      -1: X=0.50000000 Y=0.00000000 Z=0.50000000
      -1: X=0.75000000 Y=0.25000000 Z=0.50000000
      -1: X=0.00000000 Y=0.25000000 Z=0.50000000
      -1: X=0.75000000 Y=0.50000000 Z=0.50000000
      -1: X=0.75000000 Y=0.25000000 Z=0.00000000
      -1: X=0.00000000 Y=0.50000000 Z=0.00000000
      -1: X=0.25000000 Y=0.50000000 Z=0.00000000
      -1: X=0.00000000 Y=0.75000000 Z=0.00000000
      -1: X=0.00000000 Y=0.50000000 Z=0.50000000
Si1   NPT= 781 R0=.000100000 RMT= 2.00000 Z: 14.00000
LOCAL ROT MATRIX:  1.0000000 0.0000000 0.0000000
                   0.0000000 1.0000000 0.0000000
                   0.0000000 0.0000000 1.0000000
ATOM  -2: X=0.25000000 Y=0.25000000 Z=0.00000000
      MULT=16          ISPLIT=15
      -2: X=0.50000000 Y=0.50000000 Z=0.00000000
      -2: X=0.75000000 Y=0.50000000 Z=0.00000000
      -2: X=0.50000000 Y=0.75000000 Z=0.00000000
      -2: X=0.50000000 Y=0.50000000 Z=0.50000000
      -2: X=0.75000000 Y=0.75000000 Z=0.50000000
      -2: X=0.00000000 Y=0.75000000 Z=0.50000000
      -2: X=0.75000000 Y=0.00000000 Z=0.50000000
      -2: X=0.75000000 Y=0.75000000 Z=0.00000000
```

```
-2: X=0.25000000 Y=0.75000000 Z=0.50000000
-2: X=0.50000000 Y=0.75000000 Z=0.50000000
-2: X=0.25000000 Y=0.00000000 Z=0.50000000
-2: X=0.25000000 Y=0.75000000 Z=0.00000000
-2: X=0.50000000 Y=0.00000000 Z=0.00000000
-2: X=0.75000000 Y=0.00000000 Z=0.00000000
-2: X=0.50000000 Y=0.25000000 Z=0.00000000
Si2      NPT= 781  RO=.000100000 RMT= 2.00000  Z: 14.00000
LOCAL ROT MATRIX:  1.0000000 0.0000000 0.0000000
                   0.0000000 1.0000000 0.0000000
                   0.0000000 0.0000000 1.0000000
ATOM -3: X=0.06250000 Y=0.06250000 Z=0.12500000
      MULT=16          ISPLIT=15
-3: X=0.31250000 Y=0.06250000 Z=0.12500000
-3: X=0.06250000 Y=0.06250000 Z=0.62500000
-3: X=0.31250000 Y=0.31250000 Z=0.62500000
-3: X=0.56250000 Y=0.31250000 Z=0.62500000
-3: X=0.31250000 Y=0.56250000 Z=0.62500000
-3: X=0.31250000 Y=0.31250000 Z=0.12500000
-3: X=0.56250000 Y=0.56250000 Z=0.12500000
-3: X=0.81250000 Y=0.31250000 Z=0.62500000
-3: X=0.06250000 Y=0.31250000 Z=0.62500000
-3: X=0.81250000 Y=0.56250000 Z=0.62500000
-3: X=0.81250000 Y=0.31250000 Z=0.12500000
-3: X=0.06250000 Y=0.56250000 Z=0.12500000
-3: X=0.31250000 Y=0.56250000 Z=0.12500000
-3: X=0.06250000 Y=0.81250000 Z=0.12500000
-3: X=0.06250000 Y=0.56250000 Z=0.62500000
Si3      NPT= 781  RO=.000100000 RMT= 2.00000  Z: 14.00000
LOCAL ROT MATRIX:  1.0000000 0.0000000 0.0000000
                   0.0000000 1.0000000 0.0000000
                   0.0000000 0.0000000 1.0000000
ATOM -4: X=0.06250000 Y=0.31250000 Z=0.12500000
      MULT=16          ISPLIT=15
-4: X=0.81250000 Y=0.56250000 Z=0.12500000
-4: X=0.56250000 Y=0.81250000 Z=0.12500000
-4: X=0.56250000 Y=0.56250000 Z=0.62500000
-4: X=0.81250000 Y=0.81250000 Z=0.62500000
-4: X=0.06250000 Y=0.81250000 Z=0.62500000
```

C. Supercells

```
-4: X=0.81250000 Y=0.06250000 Z=0.62500000
-4: X=0.81250000 Y=0.81250000 Z=0.12500000
-4: X=0.31250000 Y=0.81250000 Z=0.62500000
-4: X=0.56250000 Y=0.81250000 Z=0.62500000
-4: X=0.31250000 Y=0.06250000 Z=0.62500000
-4: X=0.31250000 Y=0.81250000 Z=0.12500000
-4: X=0.56250000 Y=0.06250000 Z=0.12500000
-4: X=0.81250000 Y=0.06250000 Z=0.12500000
-4: X=0.56250000 Y=0.31250000 Z=0.12500000
-4: X=0.56250000 Y=0.06250000 Z=0.62500000
Si4      NPT= 781  R0=.000100000  RMT= 2.00000  Z: 14.00000
LOCAL ROT MATRIX:  1.0000000  0.0000000  0.0000000
                   0.0000000  1.0000000  0.0000000
                   0.0000000  0.0000000  1.0000000
0        NUMBER OF SYMMETRY OPERATIONS
```

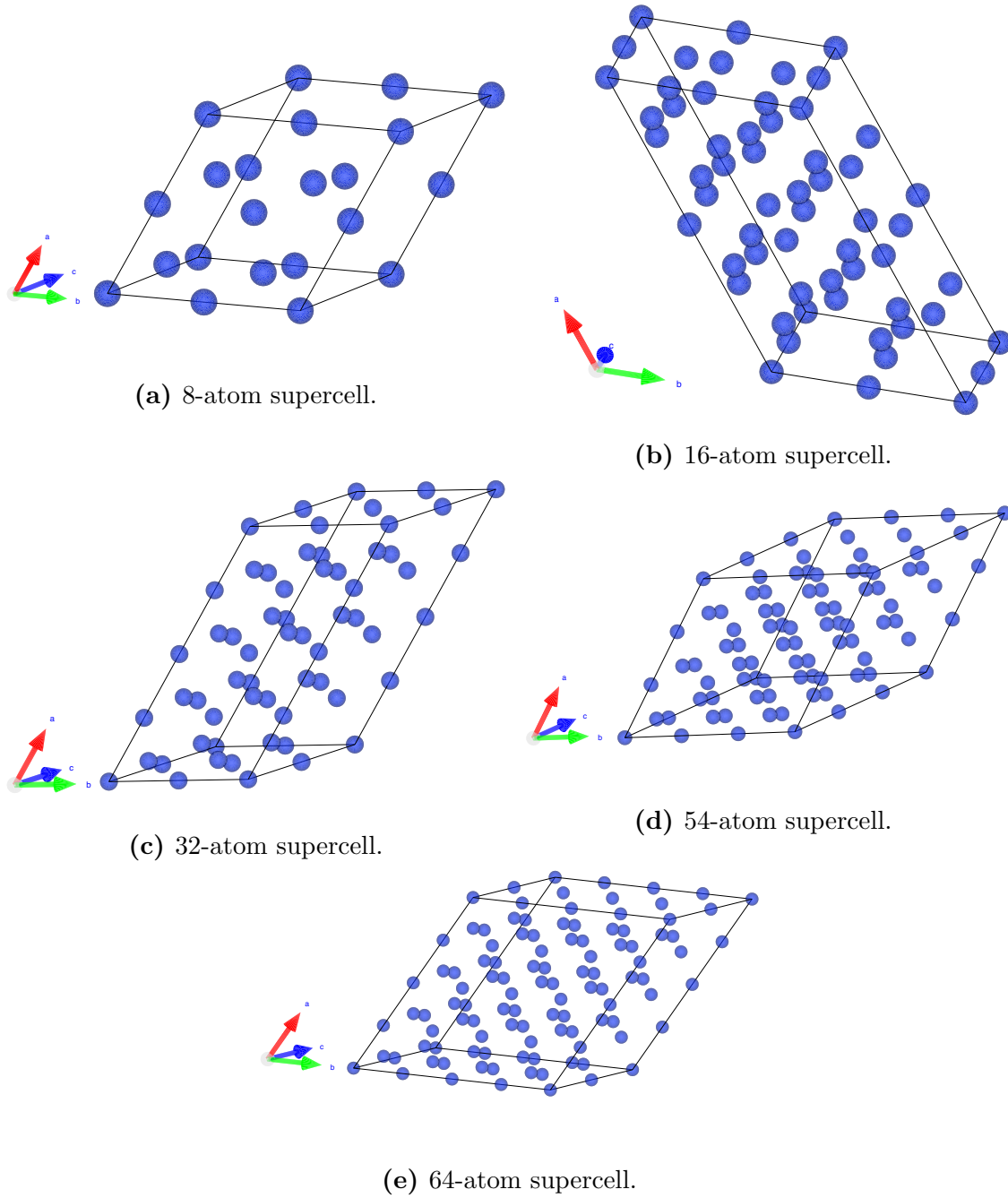


Figure C.1: Visualization of the supercells from $N=8$ to $N=64$ used for the computations, visualized using VESTA[54].

Appendix D

Convergence Tests

Convergence tests for an 8-atom supercell is shown in Figure D.1a, for a 16-atom supercell in Figure D.1b, for a 32-atom supercell in Figure D.1c, for a 54-atom supercell in Figure D.1d, and for a 64-atom supercell in Figure D.1e.

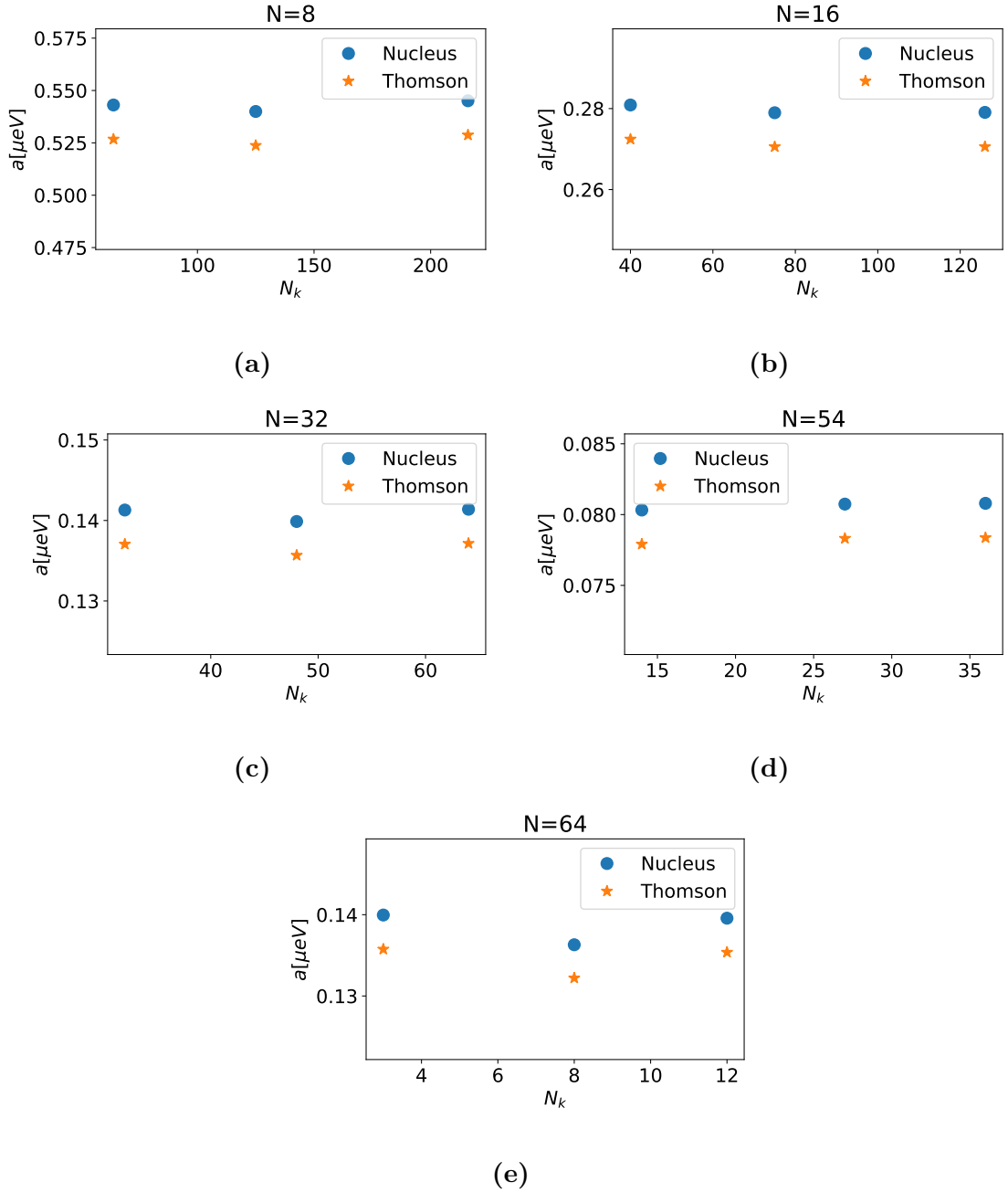


Figure D.1: Convergence tests for a , where N_k is the number of k -points in the IBZ used in the computation. The label "Nucleus" (blue dot) is for a computed using only the density at the nucleus, while the label "Thomson" (orange star) is computed using the average density around the Thomson radius.

